THE UNIVERSITY OF CHICAGO

ULTRAFAST ELECTRONIC DYNAMICS IN CORE-SHELL QUANTUM DOTS PROBED WITH DISPERSION-FREE BROADBAND TWO-DIMENSIONAL ELECTRONIC SPECTROSCOPY

A DISSERTATION SUBMITTED TO

THE FACULTY OF THE DIVISION OF THE PHYSICAL SCIENCES

IN CANDIDACY FOR THE DEGREE OF

DOCTOR OF PHILOSOPHY

DEPARTMENT OF CHEMISTRY

BY

HAIBIN ZHENG

CHICAGO, ILLINOIS

DECEMBER 2017

Table of Contents

ACKNOWLEDGEMENTS

The work presented in this dissertation was supported by the Air Force Office of Scientific Research, the Defense Advanced Research Projects Agency QuBE, the Camille and Henry Dreyfus Foundation, Defense Threat Reduction Agency, Lockheed Martin, The Univerisity of Chicago, Department of Denfense, the National Science Foundation, the National Institutes of Health, Qatar National Research Fund and the Alfred P. Sloan Foundation.

First and foremost, I wish to thank my adviser Prof. Gregory S. Engel for giving me the chance to conduct the projects described in this dissertation. As a professor, Gregcouldgive me useful academic instructions from his profound insight; as a mentor, he is an exemplary teacher and always communicates with othersin an unbelievable proper way.Greg can always make you feel not that bad even if the experimental result is indeed bad; he is also willing to make you happier when you solved a problem.Greg encourages every student to explore the unknowns and helps them to make improvement and finally access the success. The experience in Engel group would be the most precious memory in my life.

I would thank Dr. Justin R. Caram for guiding me during my first years, and building the broadband 2DES. His instruction paved a way for me to starting my own project. I would also thank Dr. Lili Wang, Dr. Brian S. Rolczynski, Dr. Peter D. Dahlberg, Nicholas E. Williams, and Ryan E. Wood. They worked with me and helped move the project forward. Lili gave me a lot of suggestions when I was working on the core-shell project. Nick and Ryan helped with the 2DES setup and taking data. I would thank all other group members in Engel group as well, for creating a scientific atmosphere in the lab.

I would thank Prof. Dmitri V. Talapin for providing me the chance to synthesis quantum dots in his lab, when I was in despair. I would also thank Dr. Yuanyuan Wang and Eric Janke giving me instructions when preparing quantum dots. Thanks to Yuanyuan, I learned how to use glove box, schlenk line, and finally got the desired quantum dots. He also helped taking TEM and Raman spectrum to characterize the quantum dots.

I would also thank Prof. Bozhi Tian to serve on my committee and his knowledge and insights help enrich my work.

Finally, I would thank my family. My parents Jianmiao Zheng and Huiqing Zhou gave me the best education that they could offer. My wife, Dr. Yan Yu is always supportive since we are undergraduate students in Beijing, came to U.S. with me, and married to me. My new born daughter, Scarlett, bring me a lot of happiness while I am working on the dissertation.

LIST OF FIGURES

LIST OF TABLES

ABSTRACT

Quantum dots are gaining increasing interest in the last three decades, due to their unique optical and electronic properties intermediate between the bulk materials and single molecules. They have a long list of potential applications including but not limited to solar cells and photovoltaics, LEDs, quantum computation, laser medium and medical imaging, because of their highly tunable properties.

In this dissertation, I prepared a series of monodispersed CdSe, CdSe/ZnS, CdSe/ZnS/CdSe quantum dots. Using the all-reflective dispersion-free broadband two dimensional electronic spectroscopy that we previously developed, I am able to probe the electronic dynamics of the first two excitons in these quantum dots at very early time. The ZnS shell influences the surface profile, and presents different relaxation dynamics in these core-shell quantum dots.

1 Introduction

Spectroscopy is the study of the interactions between electromagnetic fields and matter. It can be used to understand the microscopic interactions and dynamics. In the past two decades, two-dimensional electronic spectroscopy (2DES) has been developed, to probes photo-initiated electronic dynamics on ultrafast timescales [1-4]. It has been applied to study systems including spectral diffusion [1,5,6], photosynthetic light-harvesting [7-14], semiconducting nanocrystals [15-18] and atomic vapors [19-22]. 2DES improves resolution compared to pump-probe spectroscopies by separating homogenous and inhomogeneous broadening along distinct spectral axes [23]. The resulting 2D maps correlate excitation at a specific energy with the fate of that excitation across the entire excitation window. This approach decouples the pulse bandwidth from the frequency resolution of the experiment, which is ultimately determined by the molecular response. Thus, 2DES can exploit spectrally broad, sub-10fs, ultrafast pulses for pump and probe, while monitoring electronic and vibrational couplings and coherences across diverse chromophores and environments. 2DES accesses detailed dynamical information without the use of multiple spectrally distinct laser pulses.

Since first discovered by Alexey Ekimov in 1980, nanocrystal quantum dots (NC QDs) have gained considerable attention over the last three decades. QDs are only several nanometers in size and exhibit physical and chemical properties that are intermediate between those of bulk semiconductors and those of free molecular systems. The optical and electronic properties of QDs can be controlled by changing the chemical composition, size, and shape; this gives rise to

many potential applications for QDs in quantum computation [24-26], photovoltaic devices [27-29], light emitting devices [30-32], biological labels and medical devices [33-35].

In this chapter, I will discuss theories of non-linear spectroscopy and 2DES first, and then introduce quantum dots and quantum confinement effects briefly. In this dissertation, we developed a dispersion-free broadband two dimensional electronic spectroscopy, and used it to probe the electronic dynamics within the quantum dot systems.

1.1 Coherent spectroscopy

Spectroscopy is a measurement from the interaction between the light and matter. The propagation of light can be derived from Maxwell equation:

$$\nabla^2 \vec{E} - \frac{1}{v^2}\frac{\partial^2 \vec{E}}{\partial t^2} = 0 \tag{1.1}$$

where $\vec{E}$ is the electric field, v is the phase velocity. One solution of equation (1.1) is

$$\vec{E}(\vec{r},t) = \vec{A}e^{i(\vec{k}\cdot\vec{r}-\omega\cdot t)} + c.c. \tag{1.2}$$

where $\vec{A}$ is the amplitude of the electromagnetic field, $\vec{k}$ is the wave vector, $\vec{r}$ is the position, ω is the angular velocity and t is the time. When the light interacts with the matter, an induced dipole moment will be created:

$$\vec{P} = q\vec{d} \tag{1.3}$$

where q is the electronic charge per unit volume, and $\vec{d}$ is the displacement vector pointing from the negative charge to the positive charge. This dipole moment (polarization density) is related to the electric field:

$$\vec{P} = \vec{P}_L + \vec{P}_{NL} = \varepsilon_0\chi^{(1)}\cdot\vec{E} + \left[\varepsilon_0\chi^{(2)}\cdot\vec{E}\cdot\vec{E} + \varepsilon_0\chi^{(3)}\cdot\vec{E}\cdot\vec{E}\cdot\vec{E} + \cdots\right] \tag{1.4}$$

where ε_0 is the electric permittivity, $\chi^{(n)}$ is an n+1 rank tensor representing the n-th order electric susceptibility. The terms in brackets is non-linear polarization, while $\vec{P}_L = \varepsilon_0 \chi^{(1)} \cdot \vec{E}$ is the linear polarization. The wave equation in the polarized material is:

$$\nabla^2 \vec{E} - \mu_0 \frac{\partial^2 \vec{D}}{\partial t^2} = 0 \tag{1.5}$$

where the electric displacement $\vec{D} = \varepsilon_0 \vec{E} + \vec{P}$, and μ_0 is the permeability of vacuum. Comparing to the equation (1.1), the solution can be expressed as:

$$\vec{P}(\vec{r}, t) = \vec{P}(t) e^{i(\vec{k}_{sig} \cdot \vec{r} - \omega_{sig} \cdot t)} + c.c. \tag{1.6}$$

This polarization acts as a source of radiation, which was detected in our experiments.

For coherent spectroscopy, dipoles are driven coherently by one or more input electronic fields, and the signal is detected in a well-defined direction:

$$\overrightarrow{k_{sig}} = \pm \vec{k}_1 \pm \vec{k}_2 \pm \vec{k}_3 \cdots \pm \vec{k}_n \tag{1.7}$$

Also the signal frequency depends on the individual incident pulses:

$$\omega_{sig} = \pm \omega_1 \pm \omega_2 \pm \omega_3 \cdots \pm \omega_n \tag{1.8}$$

where $\vec{k}_i$ and ω_i are the wave vector and frequency of the i-th electronic field interacts with the material system [36].

1.2 Principles in Two Dimensional Electronic Spectroscopy

When the electric filed is very intense, the nonlinear terms in the equation (1.4) cannot be neglected. For material systems with inversion symmetry, the even orders of electric susceptibilities are zero, thus the lowest-order nonlinearity is the third-order response.

We calculate the third-order polarization from the density operator:

$$P^{(3)}(t) = Tr(\mu\rho^{(3)}(t)) \tag{1.9}$$

where μ is the dipole operator, ρ is the density operator of the system. The time evolution of a density operator can be derived using the schrödinger equation and finally yields the quantum Liouville equation (also known as the Liouville Von Neumann equation) [36]:

$$\frac{\partial\rho}{\partial t} = \frac{\partial\left|\Psi(t)\right\rangle}{\partial t}\left\langle\Psi(t)\right| + \left|\Psi(t)\right\rangle\frac{\partial\left\langle\Psi(t)\right|}{\partial t} = \frac{-i}{\hbar}\left[H,\rho\right] \tag{1.10}$$

Using perturbation theory, the Hamiltonian can be written as

$$H = H_0 + V(t) \tag{1.11}$$

where H_0 is the unperturbed Hamiltonian of no time-dependence, and V(t) is the time-dependent perturbation term. When the electronic field interacts with the system, it can be written as the product of dipole operator and electric field:

$$V(t) = -\vec{\mu}\cdot\vec{E} \tag{1.12}$$

Substituting the solution of (1.10) for the density operator, into equation (1.9), the expression for the third-order polarization at time t and a specific point in space is obtained:

$$P^{(3)}(\vec{r},t) = \int_0^\infty\int_0^\infty\int_0^\infty S^{(3)}(\tau_a,\tau_b,\tau_c)E(\vec{r},t_1)E(\vec{r},t_2)E(\vec{r},t_3)d\tau_a d\tau_b d\tau_c \tag{1.13}$$

where t_1 (t-τ_a-τ_b-τ_c), t_2 (t-τ_b-τ_c), t_3 (t-τ_c) are the times that three electric fields interacts with the system, and τ_a, τ_b, τ_c are the time delay between three pulses and the signal. The definition of these time variables is shown in the figure 1.1.

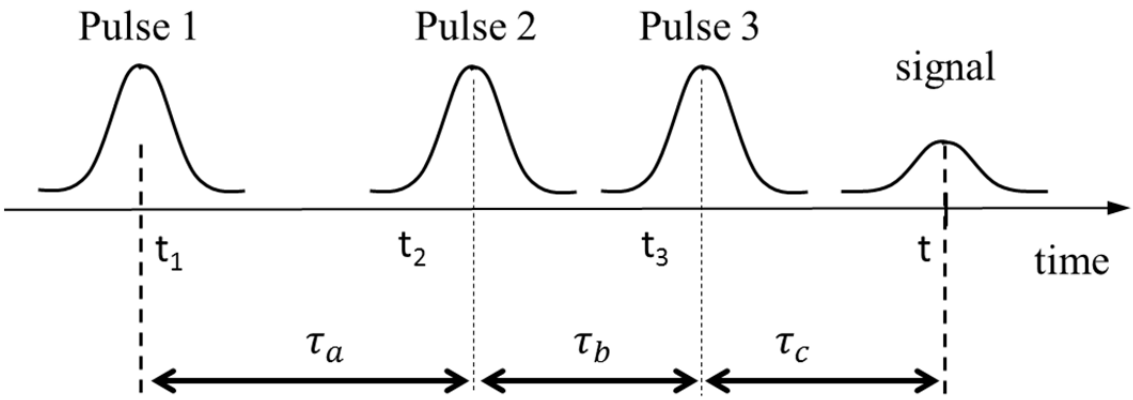

Figure 1.1 Three pulses interact with the matter to generate the third order polarization. The time variables are defined in the diagram, corresponding to the equation (1.13).

$S^{(3)}$ is the third order time dependent response function, and requires τ_a, τ_b, τ_c larger than zero to ensure causality, since light-matter interaction only happens after the corresponding radiation field. It contains both the density and dipole operators, as shown in equation (1.14)

$$S^{(3)}(\tau_a,\tau_b,\tau_c)=\left(\frac{i}{h}\right)^3 Tr\left\{\left[\left[\left[\mu(\tau_a+\tau_b+\tau_c),\mu(\tau_a+\tau_b)\right],\mu(\tau_a)\right],\mu(0)\right]\rho\right\} \tag{1.14}$$

We can tell that this third order response function is the sum of eight terms, and these terms differ by whether dipole operators actor on the *bra* or *ket* side of ρ in the order. The first term can be expended as:

$$\begin{aligned} &Tr\left\{\mu(\tau_a+\tau_b+\tau_c)\mu(\tau_a+\tau_b)\mu(\tau_a)\mu(0)\rho\right\} \\ &=Tr\left\{U_0^\dagger(\tau_a+\tau_b+\tau_c)\mu U_0(\tau_a+\tau_b+\tau_c)U_0^\dagger(\tau_a+\tau_b)\mu U_0(\tau_a+\tau_b)U_0^\dagger(\tau_a)\mu U_0(\tau_a)\mu\rho\right\} \\ &=Tr\left\{\mu\left[U_0(\tau_c)\mu\left[U_0(\tau_b)\mu\left[U_0(\tau_a)\mu\rho U_0^\dagger(\tau_a)\right]U_0^\dagger(\tau_b)\right]U_0^\dagger(\tau_c)\right]\right\} \end{aligned} \tag{1.15}$$

where U_0 is the time evolution operator. In this term, dipole operator acts on the *ket* of density matrix first, then the system evolves under H_0 during τ_a; after dipole acts on the *ket* again, the system evolves under H_0 during τ_b; then the dipole acts on the *ket* for the third time and the system evolves during τ_c; later the density matrix is multiplied by dipole operator and the trace is

calculated. This process can be illustrated using Feynman diagrams as shown in figure 1.2. In order to emphasize that the electronic field interacts on the *ket*, some details in a Feynman diagram are now drawn here.

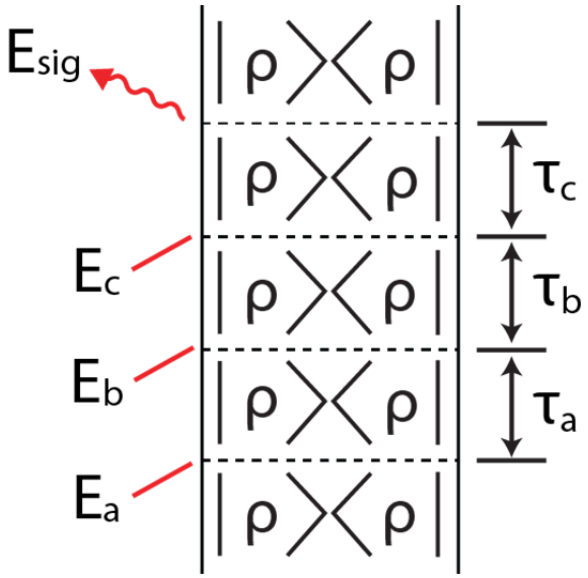

Figure 1.2 A representative Feynman diagram shows that three electronic fields interact with the system, and the dipole operator works on the *ket* three times, corresponding to the term in equation (1.15). The arrows represent that the system interactions with electronic fields. The double-sided column represents the upward time evolution of the density operator.

Feynman diagram is an easy way of tracking these interactions in various pathways (terms in equation (1.14)). As shown in the figure 1.3, for a Feynman diagram, the density operator is represented by two columns: the *ket* is on the left side, and the *bra* is on the right side. The time evolves upward in this diagram. In two dimensional electronic spectroscopy (2DES) experiment, we can control the time delay τ_a, τ_b, τ_c, which is named as coherent time (τ), waiting time (T) and rephrasing time (t), indicating the time delay between these three incident electronic fields and the signal. An interaction with the electronic field on the density matrix is represented by an arrow: Inward pointing arrows represent absorption while outward pointing arrows indicate emission. Arrows on the left side act on the *ket*, and arrows on the right side act on the *bra*. Each

diagram has an sign of $(-1)^n$ where n is the number of interactions on the *bra*, because each time an interaction acts from the right in a commutator will change the sign.

In conventional Feynman diagram, the material system starts from ground state, and ends with a population state. The last arrow pointing outwards, corresponding to the signal emitted due to the third order polarization induced by the first three interactions with the electronic fields. The arrow pointing to the left associates with a negative wave vector, and the arrow pointing to the right represents interaction with an electronic field of positive wave vector. The wave vector of the signal is the sum of three wave vectors with appropriate signs. The terms in equation (1.14) will lead to different signals with different wave vectors. In 2DES experiment, we collect the signal in the phase-matched direction, $k_s=-k_1+k_2+k_3$, and most terms in the equation (1.14) will vanish, only 6 pathways will survive and are shown in the figure 1.3. We assume that there are only three states in the system: ground state (*g*), the first excited state (*e*), and the second excited state (*f*). These 6 pathways can be differentiated as rephasing (the left three diagrams) and nonrephasing (the right three diagrams), for different time ordering of pulse 1 and pulse 2. So we can selectively detect rephasing signals via enforcing that the pulse 1 arrives earlier than pulse 2. In addition, we separate these pathways into ground state bleaching (GSB), stimulated emission (SE) and excited state absorption (ESA). Ground state bleaching refers to depletion of the charge carriers in the ground state to an excited state. The system is on the ground state during waiting time. If the system is on the first excited state after interacted with the first two pulses, it can either absorb another photon and excited to a higher excited state (ESA) or emit a photon (SE) when interacts with the third pulse. In a two-dimensional spectrum or pump-probe spectrum recording transmitted light, ground state bleaching and stimulated emission signals will create positive spectral features, while excited state absorption will create negative features.

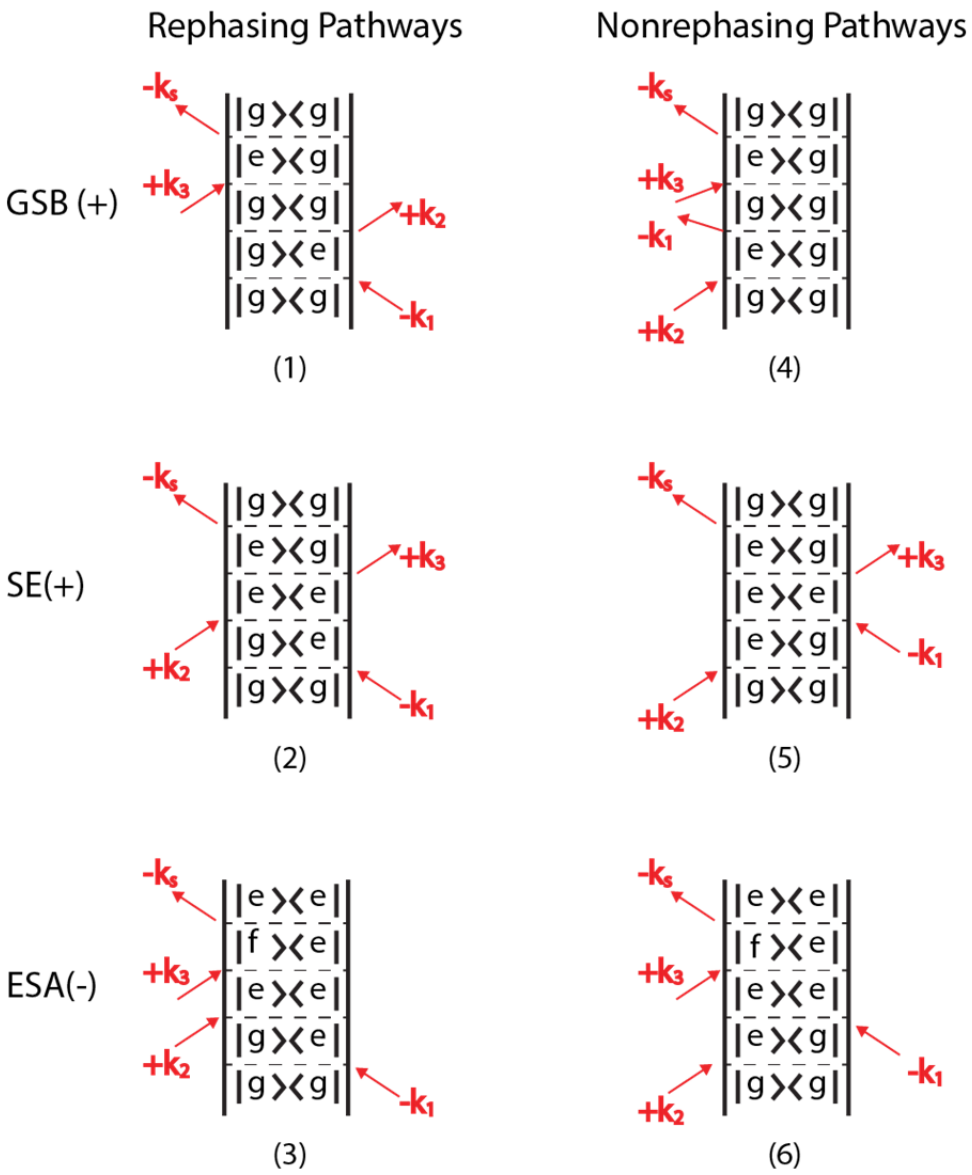

Figure 1.3 Feynman diagrams represent six different pathways generating signal in the direction k_s=-k_1+k_2+k_3. The left three diagrams correspond to rephasing pathways, and the right three diagrams represent nonrephasing response pathways. The ground state bleaching (GSB) and stimulated emission (SE) show a positive signal, while excited state absorption (ESA) shows a negative signal.

Feynman diagram can be used to analyzing spectral features in two-dimensional electronic spectrum, and explain the waiting time dynamics in 2DES. For example, we are able to monitor

the population transfer during waiting time from state b to state a, as shown in the figure 1.4. More applications of Feynman diagram in 2DES to help understanding spectral features will be discussed in the next chapters

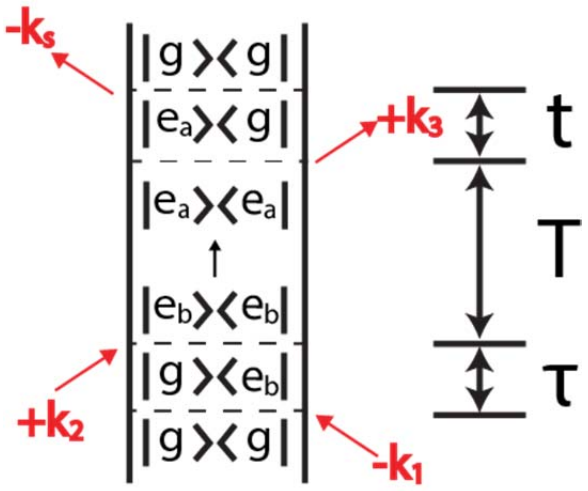

Figure 1.4 The Feynman diagram shows population transfer during waiting time T, from the excited state *b* to another excited state *a*.

1.3 Quantum dots and quantum confinement effect

In bulk semiconductor materials, the number of atoms or orbitals is very large and the energy levels are very close. The occupied electronic orbitals (valence band) and unoccupied orbitals (conduction band) can be considered as a continuum energy bands. The energy gap between the conduction band and valence band (bandgap) is a fixed parameter for a specific identity (figure 1.4, (a)). However, this situation changes when the size of the semiconductor material reduces to be less than ten nanometers. The bandgap increases compared to bulk with quantization of the

energy levels to be discrete, and the manifold of the energy levels in these nanoscale particles (quantum dots) is shown in figure 1.5 (b).

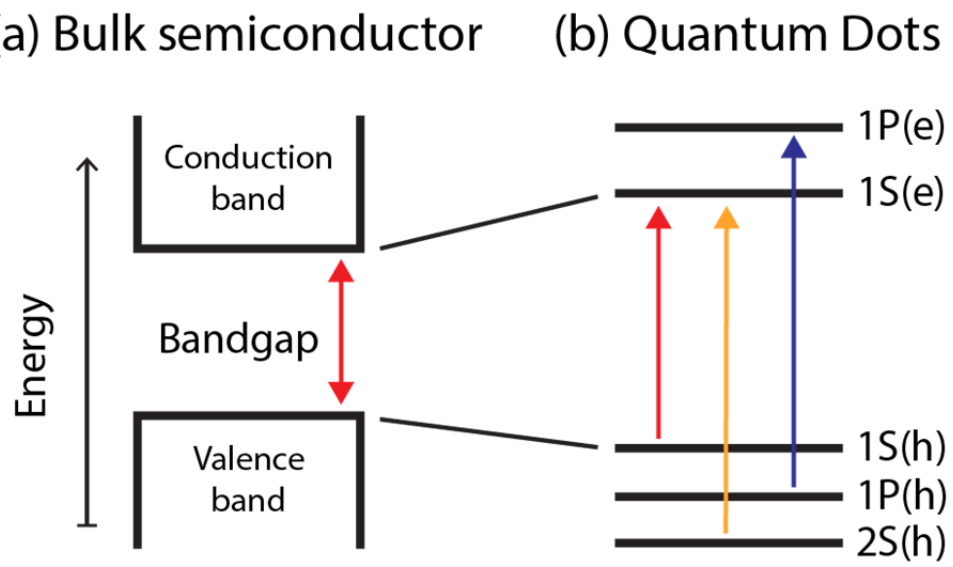

Figure 1.5 (a) A bulk semiconductor has continuous conduction band and valence band, separated by a fixed energy gap. (b) Quantum dots are characterized by discrete atomic-like energy levels.

In QDs whose size is reduced to a few nanometers, which is the same magnitude as the de Broglie wavelength of the electron wave function, the band gap increases compared to bulk with quantization of the energy levels to be discrete. This effect is known as quantum confinement effect [37]. The de Broglie wavelength of electron is given by

$$\lambda_{deB} = \frac{h}{p} = \frac{h}{\sqrt{m_e k_B T}} \tag{1.16}$$

where h is the planck constant, m_e is the mass of an electron, k_B is the Boltzmann constant, and T is the temperature. At room temperature (T = 298 K), the wavelength equals to 10 nm. So for semiconductor particles with spatial dimensions on the order of ten nanometers, quantum

confinement effect will be prominent. The motion of electron is restricted and can "feel" the presence of the particle boundaries.

The color of light emitted by the semiconductor material is determined by the width of the energy gap separating the conduction band and balance band. In a simple picture, the band gap in quantum dots (separation between the lowest electron and hole states) can be predicted using the particle in a box model [38]. Using a spherical quantum well, it can be expressed as [39]:

$$E_{QD} = E_{\text{bulk}} + E_{\text{confinement}} = E_{\text{bulk}} + \frac{h^2}{8\mu R^2} \tag{1.17}$$

where h is the planck constant, μ= memh/(me+mh) (with me and mh as the electron and hole effective masses) is the reduced mass, R is the radius of the quantum dot. This equation (1.17) implies that the electronic transition in the quantum dots highly depends on the size. Typically the energy gap increases as the particle size decreases, and this relationship in CdSe quantum dots was measured by Yu et.al [40], and re-printed with permission here in figure 1.6.

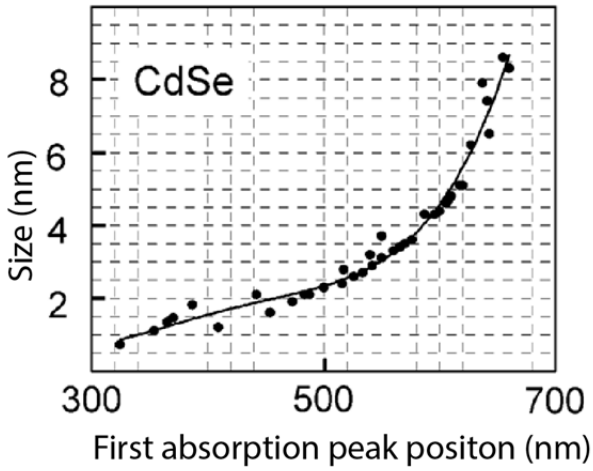

Figure 1.6 The curve shows the relationship between the energy of the first excited state and particle size for CdSe quantum dots [40].

1.4 Core-shell quantum dots

The quantum dots yield a very high surface-to-volume ratio when the size is reduced to a few nanometers. A high proportion of atoms are on the surface and coordinated with the stabilizing organic ligands. Nevertheless, surface trap states are present in these organically passivated quantum dots, providing a fast non-radiative de-excitation channel for exciton relaxations. The fluorescence quantum yield (the probability of the excited state being deactivated by fluorescence rather than by non-radiative mechanism) will diminish in these quantum dots, which challenges the applicability in future technologies [41].

One strategy to improve the surface structure and reduce surface effects is to grow a shell of a different semiconductor material, producing a core-shell structure. The shell growth reduces the surface trap states for charge carriers, via eliminating surface dangling bonds. In addition, the shell can isolate the core from the organic ligands, to reduce low-lying (near band edge) hole relaxation, which is dominated by the ligand-involved non-radiative pathway [42-44]. The shell can also be selected to enhance the stability of quantum dots and protect it against photo-oxidation. In addition, it is possible to tune the emission wavelength of the quantum dots via tuning the chemical composition and thickness of the shell layers [45].

In a special case when the bandgap of the core is within that of the shell, or in other words, the HOMO of the core is higher, and the LUMO of the core is lower, compared to those of the shell, both electrons and holes are confined in the core. Then the shell is basically used to tune the surface profile of the core, and improve the optical properties. A typical sample for this type of core-shell structure is CdSe/ZnS (the band gap is 3.61 eV for ZnS compared to 1.74 eV of CdSe). The growth of ZnS leads to a small red shift of both the absorption peak positions in UV-Vis spectrum and the emission wavelength in photoluminescence spectrum.

Furthermore, quantum dots containing multiple shells were developed to optimize electronic and structural parameters. For example, CdSe/ZnSe/ZnS and CdSe/CdS/ZnS were obtained by Talapin in 2004 [46]. By introducing the ZnSe or CdS, the strain within the quantum dots, especially at the interface, will be significantly reduced, since the lattice mismatch between ZnS and CdSe is mediated by the middle layers. In 2005, Battaglia et.al synthesized a series of CdSe/ZnS/CdSe core-shell-shell quantum dots, and successfully realized tuning the electronic coupling between the core and the outside CdSe shell, by alteration of the thickness of the ZnS barrier layer [47].

1.5 Ultrafast electronic dynamics of Quantum dots

The electronic dynamics, such as relaxation processes of high energy photo-excitations (hot exciton) have been studied using ultrafast nonlinear spectroscopies. Using transient absorption (TA) [48-50], photon echo peak shift [51, 52] or two-dimensional electronic spectroscopy (2DES) [17, 18, 53, 54], the quantum dots will first be initiated to high energy excitonic states and then the underlying physical process will be probed. In CdSe quantum dots, the hot exciton relaxes rapidly after excitation on femto-second time scale [17]. A few mechanisms have been proposed to explain the fast energy relaxation in QDs: (1) an Auger-like mechanism, when the excited electron transits to a lower energy level, with a hot hole relaxation through its manifold towards the band edge or to a trap state [55, 56]; (2) surface process, including surface defects or passivating ligands leads to intermediate states with coupling between electron and molecular vibrations or lattice phonon [42, 57].

REFERENCES

[1] J.D. Hybl, A.A. Ferro, D.M. Jonas, Two-dimensional Fourier transform electronic spectroscopy, J Chem Phys, 115 (2001) 6606-6622.

[2] D.M. Jonas, Two-Dimensional Femtosecond Spectroscopy, Annual Review of Physical Chemistry, 54 (2003) 425-463.

[3] M.L. Cowan, J.P. Ogilvie, R.J.D. Miller, Two-dimensional spectroscopy using diffractive optics based phased-locked photon echoes, Chem Phys Lett, 386 (2004) 184-189.

[4] T. Brixner, T. Mancal, I. Stiopkin, G. Fleming, Phase-stabilized two-dimensional electronic spectroscopy, J Chem Phys, 121 (2004) 4221-4236.

[5] K. Wells, Z. Zhang, J. Rouxel, H. Tan, Measuring the Spectral Diffusion of Chlorophyll a Using Two-Dimensional Electronic Spectroscopy, Journal of Physical Chemistry B, 117 (2013) 2294-2299.

[6] J.D. Hybl, A. Yu, D.A. Farrow, D.M. Jonas, Polar Solvation Dynamics in the Femtosecond Evolution of Two-Dimensional Fourier Transform Spectra, J. Phys. Chem. A, 106 (2002) 7651-7654.

[7] T. Brixner, J. Stenger, H.M. Vaswani, M. Cho, R.E. Blankenship, G.R. Fleming, Two-dimensional spectroscopy of electronic couplings in photosynthesis, Nature, 434 (2005) 625-628.

[8] G.S. Engel, T.R. Calhoun, E.L. Read, T.-K. Ahn, T. Mancal, Y.-C. Cheng, R.E. Blankenship, G.R. Fleming, Evidence for wavelike energy transfer through quantum coherence in photosynthetic systems, Nature, 446 (2007) 782-786.

[9] E. Read, G. Engel, T. Calhoun, T. Mancal, T. Ahn, R. Blankenship, G. Fleming, Cross-peak-specific two-dimensional electronic spectroscopy, Proceedings of the National Academy of Sciences of the United States of America, 104 (2007) 14203-14208.

[10] E. Collini, C.Y. Wong, K.E. Wilk, P.M.G. Curmi, P. Brumer, G.D. Scholes, Coherently wired light-harvesting in photosynthetic marine algae at ambient temperature, Nature, 463 (2010) 644-647.

[11] G. Schlau-Cohen, A. Ishizaki, G. Fleming, Two-dimensional electronic spectroscopy and photosynthesis: Fundamentals and applications to photosynthetic light-harvesting, Chem Phys, 386 (2011) 1-22.

[12] N. Ginsberg, J. Davis, M. Ballottari, Y. Cheng, R. Bassi, G. Fleming, Solving structure in the CP29 light harvesting complex with polarization-phased 2D electronic spectroscopy, Proceedings of the National Academy of Sciences of the United States of America, 108 (2011) 3848-3853.

[13] E. Harel, G.S. Engel, Quantum coherence spectroscopy reveals complex dynamics in bacterial light-harvesting complex 2 (LH2), Proceedings of the National Academy of Sciences of the United States of America, (2012).

[14] E.E. Ostroumov, R.M. Mulvaney, R.J. Cogdell, G.D. Scholes, Broadband 2D Electronic Spectroscopy Reveals a Carotenoid Dark State in Purple Bacteria, Science, 340 (2013) 52-56.

[15] G. Moody, R. Singh, H. Li, I.A. Akimov, M. Bayer, D. Reuter, A.D. Wieck, A.S. Bracker, D. Gammon, S.T. Cundiff, Influence of confinement on biexciton binding in semiconductor quantum dot ensembles measured with two-dimensional spectroscopy, Phys. Rev. B: Condens. Matter, 87 (2013) 041304.

[16] C. Wong, G. Scholes, Biexcitonic Fine Structure of CdSe Nanocrystals Probed by Polarization-Dependent Two-Dimensional Photon Echo Spectroscopy, Journal of Physical Chemistry a, 115 (2011) 3797-3806.

[17] D. Turner, Y. Hassan, G. Scholes, Exciton Superposition States in CdSe Nanocrystals Measured Using Broadband Two-Dimensional Electronic Spectroscopy, Nano Letters, 12 (2012) 880-886.

[18] G. Griffin, S. Ithurria, D. Dolzhnikov, A. Linkin, D. Talapin, G. Engel, Two-dimensional electronic spectroscopy of CdSe nanoparticles at very low pulse power, J Chem Phys, 138 (2013).

[19] P. Tian, D. Keusters, Y. Suzaki, W.S. Warren, Femtosecond Phase-Coherent Two-Dimensional Spectroscopy, Science, 300 (2003) 1553-1555.

[20] X. Dai, A. Bristow, D. Karaiskaj, S. Cundiff, Two-dimensional Fourier-transform spectroscopy of potassium vapor, Phys. Rev. A: At. Mol. Opt. Phys., 82 (2010).

[21] P.F. Tekavec, G.A. Lott, A.H. Marcus, Fluorescence-detected two-dimensional electronic coherence spectroscopy by acousto-optic phase modulation, J. Chem. Phys., 127 (2007) 214307-214321.

[22] H. Li, A.D. Bristow, M.E. Siemens, G. Moody, S.T. Cundiff, Unraveling quantum pathways using optical 3D Fourier-transform spectroscopy, Nat Commun, 4 (2013) 1390.

[23] M. Cho, Coherent Two-Dimensional Optical Spectroscopy, Chem. Rev., 108 (2008) 1331-1418.

[24] D. Loss, D. DiVincenzo, Quantum computation with quantum dots, Physical Review a, 57 (1998) 120-126.

[25] H. Kamada, H. Gotoh, Quantum computation with quantum dot excitons, Semiconductor Science and Technology, 19 (2004) S392-S396.

[26] M. House, I. Bartlett, P. Pakkiam, M. Koch, E. Peretz, J. van der Heijden, T. Kobayashi, S. Rogge, M. Simmons, High-Sensitivity Charge Detection with a Single-Lead Quantum Dot for Scalable Quantum Computation, Physical Review Applied, 6 (2016).

[27] A. Ip, S. Thon, S. Hoogland, O. Voznyy, D. Zhitomirsky, R. Debnath, L. Levina, L. Rollny, G. Carey, A. Fischer, K. Kemp, I. Kramer, Z. Ning, A. Labelle, K. Chou, A. Amassian, E. Sargent, Hybrid passivated colloidal quantum dot solids, Nature Nanotechnology, 7 (2012) 577-582.

[28] C. Chuang, P. Brown, V. Bulovic, M. Bawendi, Improved performance and stability in quantum dot solar cells through band alignment engineering, Nature Materials, 13 (2014) 796-801.

[29] Z. Ning, O. Voznyy, J. Pan, S. Hoogland, V. Adinolfi, J. Xu, M. Li, A. Kirmani, J. Sun, J. Minor, K. Kemp, H. Dong, L. Rollny, A. Labelle, G. Carey, B. Sutherland, I. Hill, A. Amassian, H. Liu, J. Tang, O. Bakr, E. Sargent, Air-stable n-type colloidal quantum dot solids, Nature Materials, 13 (2014) 822-828.

[30] P. Anikeeva, J. Halpert, M. Bawendi, V. Bulovic, Quantum Dot Light-Emitting Devices with Electroluminescence Tunable over the Entire Visible Spectrum, Nano Letters, 9 (2009) 2532-2536.

[31] L. Qian, Y. Zheng, J. Xue, P. Holloway, Stable and efficient quantum-dot light-emitting diodes based on solution-processed multilayer structures, Nature Photonics, 5 (2011) 543-548.

[32] X. Dai, Z. Zhang, Y. Jin, Y. Niu, H. Cao, X. Liang, L. Chen, J. Wang, X. Peng, Solution-processed, high-performance light-emitting diodes based on quantum dots, Nature, 515 (2014) 96-99.

[33] M. Dahan, S. Levi, C. Luccardini, P. Rostaing, B. Riveau, A. Triller, Diffusion dynamics of glycine receptors revealed by single-quantum dot tracking, Science, 302 (2003) 442-445.

[34] X. Michalet, F. Pinaud, L. Bentolila, J. Tsay, S. Doose, J. Li, G. Sundaresan, A. Wu, S. Gambhir, S. Weiss, Quantum dots for live cells, in vivo imaging, and diagnostics, Science, 307 (2005) 538-544.

[35] S. Rosenthal, J. Chang, O. Kovtun, J. McBride, I. Tomlinson, Biocompatible Quantum Dots for Biological Applications, Chemistry & Biology, 18 (2011) 10-24.

[36] S. Mukamel, Principles of nonlinear optical spectroscopy, Oxford, New York, 1995.

[37] W. Buhro, V. Colvin, Semiconductor nanocrystals - Shape matters, Nature Materials, 2 (2003) 138-139.

[38] L. Brus, Electron electron and electron-hole interactions in small semiconductor crystallites - The size dependence of the lowest excited electronic state, Journal of Chemical Physics, 80 (1984) 4403-4409.

[39] V.I. Klimov, Nanocrystal Quantum Dots, CRC Press; 2 edition2010.

[40] W. Yu, L. Qu, W. Guo, X. Peng, Experimental determination of the extinction coefficient of CdTe, CdSe, and CdS nanocrystals, Chemistry of Materials, 15 (2003) 2854-2860.

[41] A. Almeida, A. Sahu, A. Riedinger, D. Norris, M. Brandt, M. Stutzmann, R. Pereira, Charge Trapping Defects in CdSe Nanocrystal Quantum Dots, Journal of Physical Chemistry C, 120 (2016) 13763-13770.

[42] P. Guyot-Sionnest, B. Wehrenberg, D. Yu, Intraband relaxation in CdSe nanocrystals and the strong influence of the surface ligands, Journal of Chemical Physics, 123 (2005).

[43] R. Cooney, S. Sewall, K. Anderson, E. Dias, P. Kambhampati, Breaking the phonon bottleneck for holes in semiconductor quantum dots, Physical Review Letters, 98 (2007).

[44] P. Kambhampati, Unraveling the the Structure and Dynamics of Excitons in Semiconductor Quantum Dots, Accounts of Chemical Research, 44 (2011) 1-13.

[45] D. Talapin, A. Rogach, A. Kornowski, M. Haase, H. Weller, Highly luminescent monodisperse CdSe and CdSe/ZnS nanocrystals synthesized in a hexadecylamine-trioctylphosphine oxide-trioctylphospine mixture, Nano Letters, 1 (2001) 207-211.

[46] D. Talapin, I. Mekis, S. Gotzinger, A. Kornowski, O. Benson, H. Weller, CdSe/CdS/ZnS and CdSe/ZnSe/ZnS core-shell-shell nanocrystals, Journal of Physical Chemistry B, 108 (2004) 18826-18831.

[47] D. Battaglia, B. Blackman, X. Peng, Coupled and decoupled dual quantum systems in one semiconductor nanocrystal, Journal of the American Chemical Society, 127 (2005) 10889-10897.

[48] V. Klimov, Optical nonlinearities and ultrafast carrier dynamics in semiconductor nanocrystals, Journal of Physical Chemistry B, 104 (2000) 6112-6123.

[49] C. Burda, S. Link, M. Mohamed, M. El-Sayed, The relaxation pathways of CdSe nanoparticles monitored with femtosecond time-resolution from the visible to the IR: Assignment of the transient features by carrier quenching, Journal of Physical Chemistry B, 105 (2001) 12286-12292.

[50] E. McArthur, A. Morris-Cohen, K. Knowles, E. Weiss, Charge Carrier Resolved Relaxation of the First Excitonic State in CdSe Quantum Dots Probed with Near-Infrared Transient Absorption Spectroscopy, Journal of Physical Chemistry B, 114 (2010) 14514-14520.

[51] M. Salvador, P. Nair, M. Cho, G. Scholes, Interaction between excitons determines the non-linear response of nanocrystals, Chemical Physics, 350 (2008) 56-68.

[52] L. McKimmie, C. Lincoln, J. Jasieniak, T. Smith, Three-Pulse Photon Echo Peak Shift Measurements of Capped CdSe Quantum Dots, Journal of Physical Chemistry C, 114 (2010) 82-88.

[53] J. Caram, H. Zheng, P. Dahlberg, B. Rolczynski, G. Griffin, A. Fidler, D. Dolzhnikov, D. Talapin, G. Engel, Persistent Interexcitonic Quantum Coherence in CdSe Quantum Dots, Journal of Physical Chemistry Letters, 5 (2014) 196-204.

[54] B. Sun, B.A. Diogo, R. Singh, G.M. Diederich, M.E. Siemens, L.A. Padilha, W.K. Bae, J. Pietryga, V. Klimov, S. Cundiff, Two Dimensional Coherent Spectroscopy of CdSe/ZnS Colloidal Quantum Dots at Cryogenic Temperatures, CLEO: 2015, (2015) JW2A.54.

[55] A. Efros, V. Kharchenko, M. Rosen, BREAKING THE PHONON BOTTLENECK IN NANOMETER QUANTUM DOTS - ROLE OF AUGER-LIKE PROCESSES, Solid State Communications, 93 (1995) 281-284.

[56] V. Klimov, A. Mikhailovsky, D. McBranch, C. Leatherdale, M. Bawendi, Mechanisms for intraband energy relaxation in semiconductor quantum dots: The role of electron-hole interactions, Physical Review B, 61 (2000) 13349-13352.

[57] V. Klimov, A. Mikhailovsky, S. Xu, A. Malko, J. Hollingsworth, C. Leatherdale, H. Eisler, M. Bawendi, Optical gain and stimulated emission in nanocrystal quantum dots, Science, 290 (2000) 314-317.

2. Quantum Dots Preparation and Characterizations

We synthesized two different types of CdSe quantum dots for different purpose. Dr. Dolzhnikov prepared a large Zinc-blende CdSe (6.0 nm in diameter), which was used as the test sample for the dispersion-free all-reflective two-dimensional electronic spectroscopy. Haibin Zheng prepared a series of CdSe (5.1 nm) core, CdSe/ZnS (5.8 nm) core-shell, CdSe/ZnS/CdSe (7.5 nm) core-shell-shell and CdSe (6.0 nm) core, CdSe/ZnS (6.6 nm) core-shell quantum dots, to probe the early time electronic dynamics, and explore the surface effects in these samples.

2.1 Chemicals

Cadmium oxide (CdO), oleic acid (OA), 1-octadecene (ODE), selenium powder (Se), trioctylphosphine (TOP), zinc oxide (ZnO), sulfur powder (S), oleylamine (OAm), selenium dioxide (SeO_2), cadmium myristate ($Cd(myr)_2$),

2.2 CdSe, CdSe/ZnS, and CdSe/ZnS/CdSe nanocrystals

Two groups of QDs were synthesized in Prof. Talapin's lab. The series of CdSe (5.1 nm) core, CdSe/ZnS (5.8 nm) core-shell, CdSe/ZnS/CdSe (7.5 nm) were prepared first. However, when using the larger CdSe core (6.0 nm), we did not get the core-shell-shell structure successfully, due to the lattice mismatch among CdSe and ZnS, and the large surface strain.

2.2.1 Synthesis of CdSe, CdSe/ZnS, and CdSe/ZnS/CdSe

Cadmium oleate ($Cd(OAc)_2$) stock solution was prepared by mixing 0.4 mmol of CdO with 2.4 ml of OA and 20 ml of ODE in a 50-ml three-neck flask. The mixture was heated to 150 °C under vacuum and stirred by magnetic stir bar for 1 hour to eliminate the trace amount of water and O_2. After refilling with N_2, the reddish mixture was then heated to 250 °C, where the suspension became a colorless solution. Subsequently, the flask was cooled to room temperature, and the resulting $Cd(OAc)_2$ was stocked as a colorless solution for further usage.

Zinc oleate ($Zn(OAc)_2$) stock solution was prepared under the same general conditions as those used in the $Cd(OAc)_2$ synthesis, except for the zinc precursor. In a typical procedure, 2.0 mmol of ZnO, 5 ml of OA and 20 ml of ODE was loaded into a 50ml round-bottom flask and vacuum-dried at 100 °C to remove any trace oxygen. The flask was then heated to 250 °C under N_2 atmosphere till the white mixture turned to a colorless solution, indicating a completed reaction and the formation of $Zn(OA)_2$. The resulting $Zn(OAc)_2$ was later stocked as a waxy solid after the colorless solution cooling to room temperature.

Sulfur precursor (S-ODE) was obtained by dissolving 1.0 mmol of S powder in 25 ml ODE at 100 °C in N_2. Selenium precursor (TOP-Se) was prepared by dissolving 0.4 mmol Se powder in 5 ml ODE and 0.4 mL TOP. Both S-ODE and TOP-Se precursors were stocked in the glove box.

The wurtzite structure of CdSe nanocrystal (NC) core was synthesized following a classic procedure [1, 2] via successive ion layer adsorption and reaction (SILAR) method. $Cd(OAc)_2$ (0.2 mmol) stock solution was loaded into a three-neck flask and dried at 100 °C under vacuum for 1 hour. Then the colorless solution was heated to 280 °C in N_2, where 2.0 ml of OAm and TOP-Se (0.2 mmol) solution were quickly injected successively. After 10 minutes, 0.06 mmol of

$Cd(OAc)_2$ and 0.06 mmol of TOP-Se were loaded into separate syringes and injected to the flask successively. This procedure was repeated several times until CdSe NCs core reached the desired size [3], which was monitored via measuring the UV-Vis absorption spectrum of aliquots taken from the reaction solution. The size of the CdSe QDs was inferred using the curve shown in figure 1.6. A portion of the resulting Wz-CdSe NCs was washed using ethanol, and dissolved in toluene.

The CdSe/ZnS NCs and CdSe/ZnS/CdSe NCs were synthesized using this small-core as seeds, using a modified seeded-growth [4, 5] method originally described by Battaglia [6]. In a typical reaction, the as-synthesized Wz-CdSe NCs (0.04 mmol) solution was cooled to room temperature and transferred to another flask without purification. The solution was first vacuumed under 100 °C, and then refilled with N_2 and heated to 220 °C. For growth of ZnS shell, a calculated amount (based on the quantity and size of QDs [1]) of $Zn(OAc)_2$ was injected first followed by the ODE-S precursor 5 minutes later. The concentration of QDs was calculated based on the extinction coefficient (ϵ), which is estimated using empirical function in equation 2.1 [7]:

$$\varepsilon = 5857 \cdot D^{2.65} \tag{2.1}$$

where D is the diameter of the nanocrystal. Aliquots were taken from the original solution with a certain time interval for absorption measurements to monitor the reaction. After 20 minutes, the reaction stopped and the flask was allowed to cool to the room temperature. The resulting CdSe/Zns NCs were purified using anhydrous ethanol and toluene for several precipitation-redispersion cycles, and the purified NCs were dissolved in toluene, To synthesize CdSe/ZnS/CdSe NCs, the aforementioned CdSe/ZnS NCs were kept in original reaction solution at 200 °C in N2, into which a calculated amount of Cd(OAc)2 and TOP-Se precursors were

added in the same manner as that of ZnS layers growth. After 20 minutes, the reaction was stopped and cooled to room temperature. Toluene and ethanol were added to precipitate NCs and the final CdSe/ZnS/CdSe NCs were dissolved in toluene for future usage. The actual sizes of these NCs were measured using a transmission electron microscope.

A relatively small CdSe quantum dots (5.1 nm in diameter) was prepared initially. Based on this core structure, a CdSe/ZnS core-shell structure (5.8 nm) and CdSe/ZnS/CdSe core-shell-shell structure (7.5 nm) were synthesized. Another larger CdSe core (6.0 nm) and CdSe/ZnS core-shell (6.6 nm) were prepared separately.

2.2.2 Characterizations of CdSe, CdSe/ZnS, and CdSe/ZnS/CdSe

Transmission electron microscopy (TEM) images were obtained using a FEI Tecnai F30 microscope operated at 300 kV. UV-Vis absorption and photoluminescence (PL) spectra of QD dispersions were recorded using a Cary 5000 UV-Vis-NIR spectrophotometer and FluoroMax-4 spectrofluorometer (HORIBA Jobin Yvon), respectively.

The TEM images are shown in the figure 2.1. The size increases after the growth of shell layers with a narrow distribution (~3% Std). The UV-Vis spectra of the smaller quantum dots are plotted in the figure 2.2. I fit each spectrum using three Gaussian components and a cubic back ground curve [3]:

$$\mathrm{A}(\lambda) = \sum_{i=1}^{3} a_i e^{\frac{-(\lambda - x_i)^2}{2\sigma_i^2}} + \sum_{j=0}^{3} b_j \lambda^j \tag{2.2}$$

where x_i is the center position for the first three excitations, a_i is the amplitude of each Gaussian component, σ_i is the standard deviation, b_j is the coefficient in polynomial expression. The fitting parameters are listed in the table 2.1 and the results are plotted in the figure 2.2 as black dashed

lines. These monodispersed quantum dots provided a clear energy assignment for these lower laying excitons. The more detailed UV-Vis absorption spectra and PL spectra of all five quantum dots are displayed in figure 2.3. The Raman spectrum of each sample was shown in figure 2.4, showing a strong phonon mode at 210 cm^{-1}.

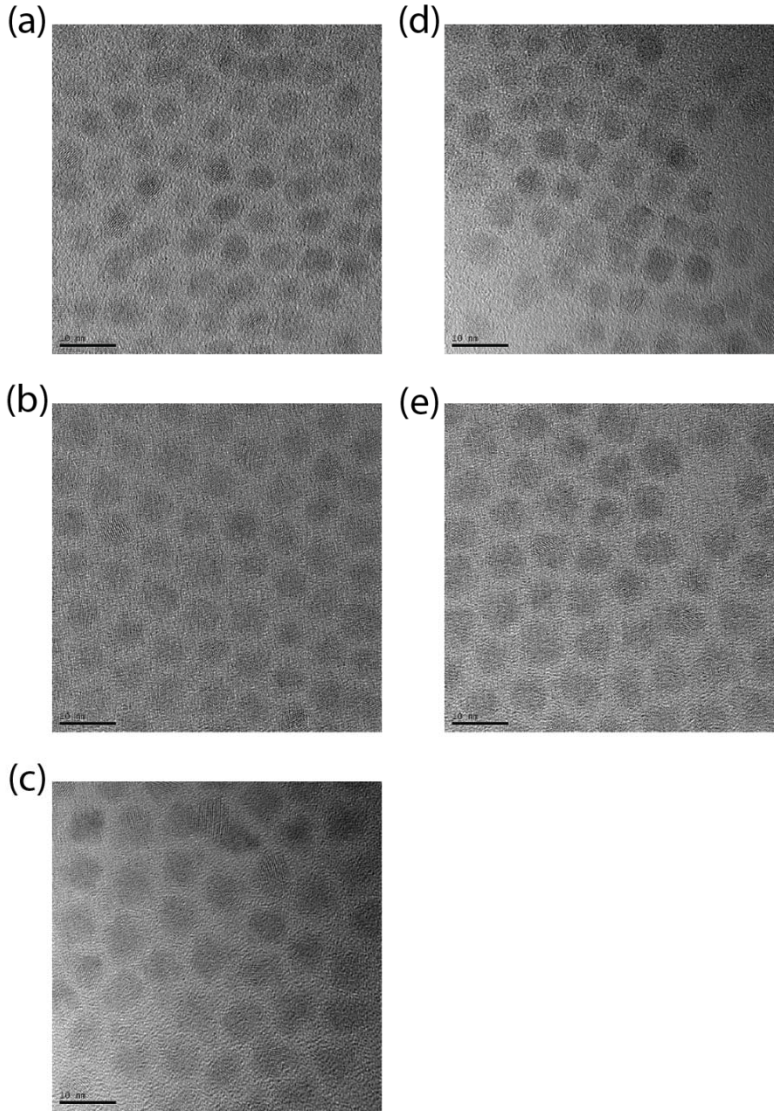

Figure 2.1 TEM images for five quantum dots. (a) CdSe (5.1 nm), (b) CdSe/ZnS (5.8 nm) and (c) CdSe/ZnS/CdSe (7.5 nm); (d) CdSe (6.0 nm) and (e) CdSe/ZnS (6.6 nm). The scale bar indicates 10 nm for all pictures.

Table 2.1 Fitting parameters for linear absorption spectra

Sample	a_1	a_2	a_3	x_1	x_2	x_3	σ_1	σ_2	σ_3	b_0	b_1	b_2 ($\times 10^{-4}$)	b_3 ($\times 10^{-8}$)
CdSe	0.179	0.075	0.058	612.9	582.3	534.1	11.4	10.8	13.0	24.1	-0.110	1.69	-8.63
CdSe/ZnS	0.168	0.064	0.053	614.5	582.4	536.3	11.8	9.88	14.2	14.7	-0.063	0.895	-4.22
CdSe/ZnS/ CdSe	0.097	0.055	0.080	623.7	592.5	556.0	11.8	10.9	22.2	20.2	-0.090	1.34	-6.58

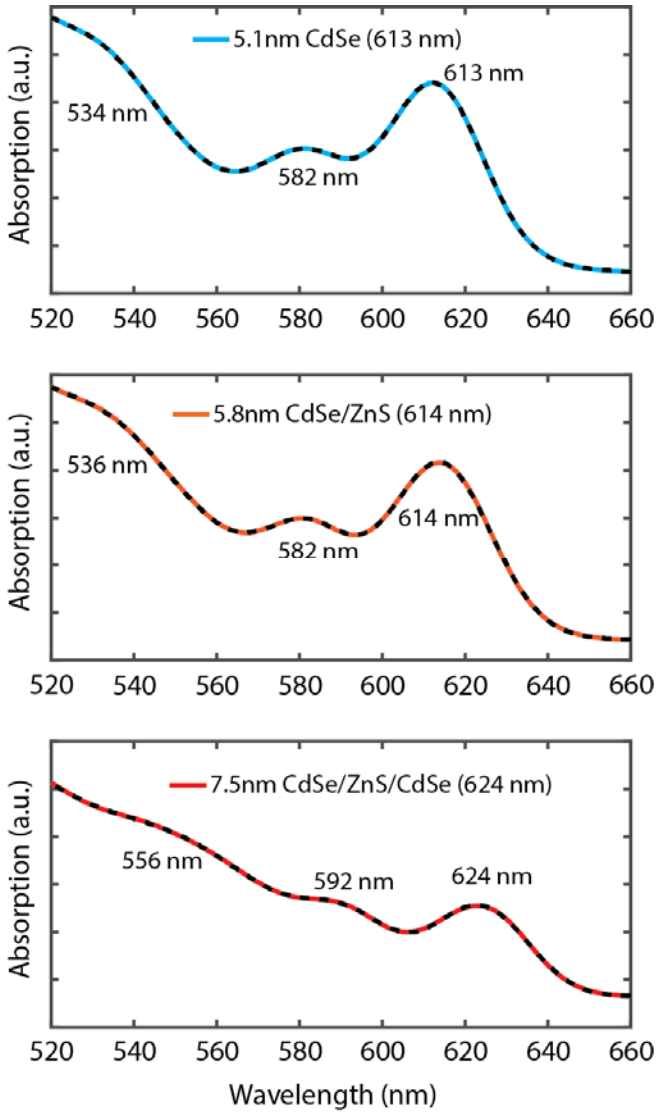

Figure 2.2 Fitting UV-Vis spectrum to three Gaussian components and a cubic back ground curve. The black dashed lines are the fitting results for these three QDs. The peak positions of three Gaussian distribution reveal the excitation energies of three lowest-energy excitons.

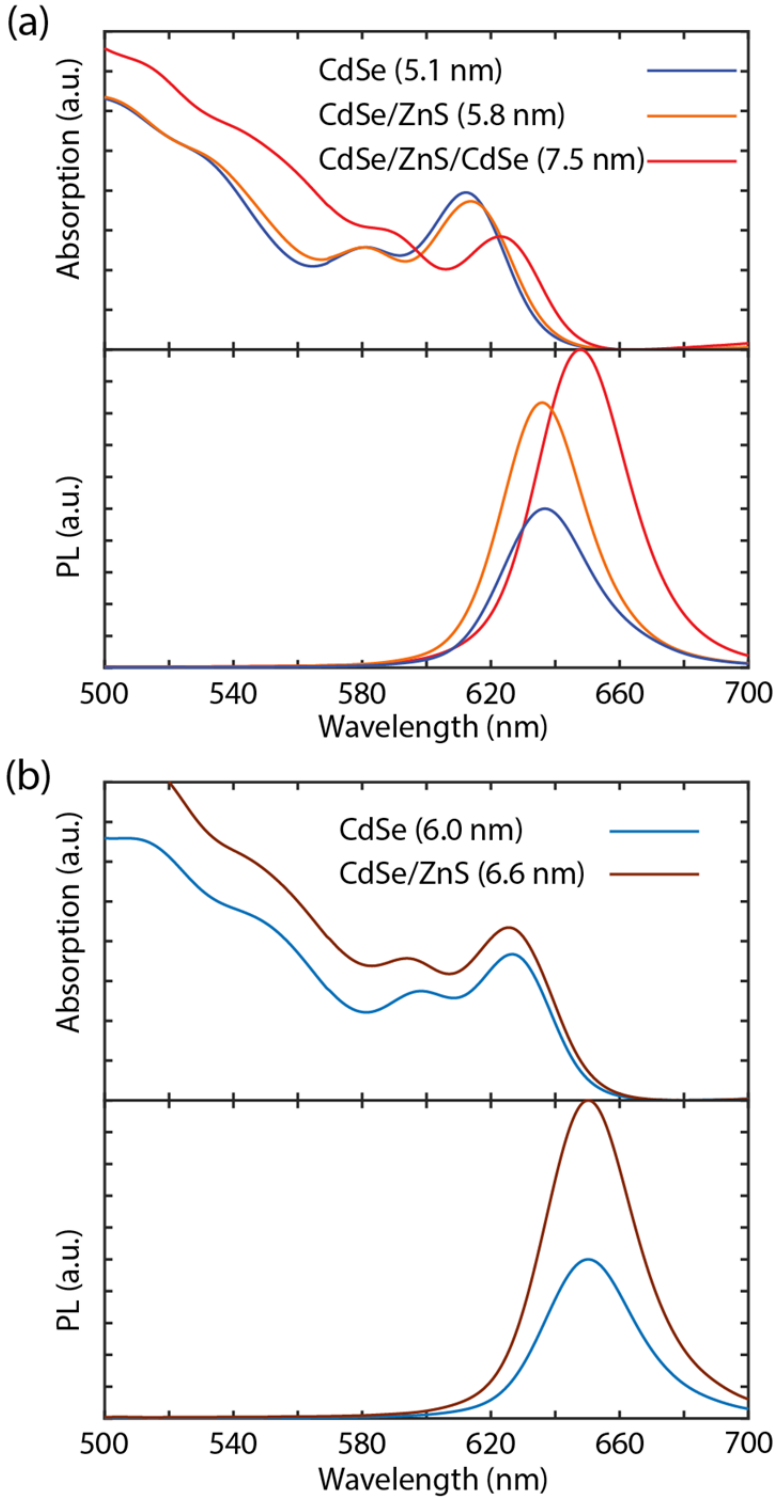

Figure 2.3 (a) UV-Vis and PL spectra of CdSe (5.1 nm) core, CdSe/ZnS (5.8 nm) core-shell, and CdSe/ZnS/CdSe (7.5 nm) core-shell-shell quantum dots. (b) UV-Vis and PL spectra of CdSe (6.0 nm) core, CdSe/ZnS (6.6 nm) core-shell quantum dots.

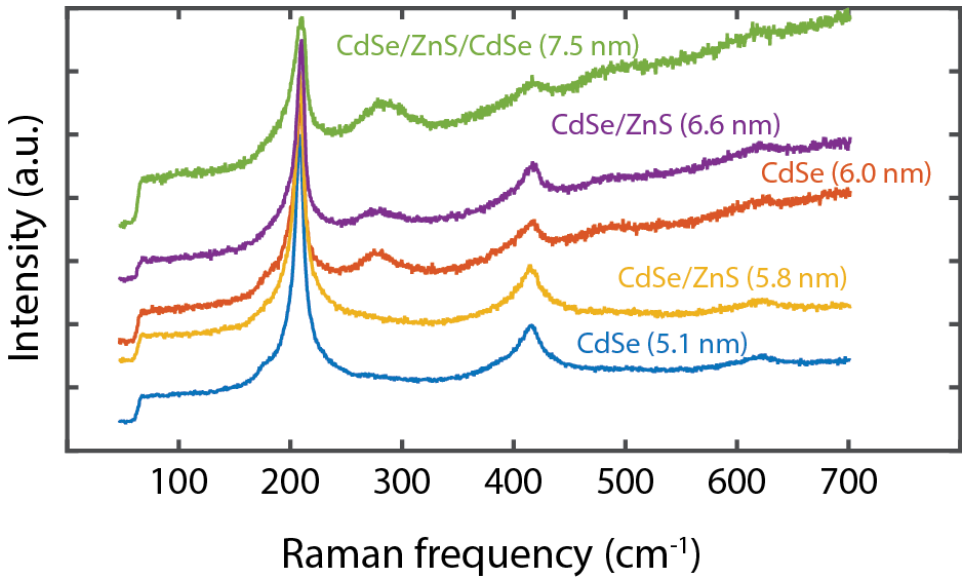

Figure 2.4 Raman spectra of all five QDs: CdSe (5.1 nm, blue), CdSe/ZnS (5.8 nm, brown) and CdSe/ZnS/CdSe (7.5 nm, orange); CdSe (6.0 nm, purple) and (e) CdSe/ZnS (6.6 nm, green). A strong phonon mode at 210 cm-1 was observed for all samples.

2.3 Synthesis of larger CdSe quantum dots and its characterizations

Larger zinc-blende CdSe quantum dots were used as a reference sample to illustrate the utility of the ultra-broadband electronic spectroscopy. It was synthesized using a different method. 0.2 mmol of $Cd(myr)_2$, 0.2 mmol of SeO_2 and 0.04 mmol of $Cd(OAc)_2$ were mixed in 12.6 mL of ODE according to a literature procedure [8]. The mixture was stirred and heated to 240 °C (heat rate ca. 20 °C /min). When the temperature reached 230 °C, 0.2 mL of oleic acid was added to ensure stable growth of nanocrystals. After an hour the solution was cooled to room temperature. Quantum dots were precipitated with ethanol and re-dispersed in toluene. Washing was repeated 2 times.

The TEM image of this CdSe shows the size of 6.0±0.6 nm (figure 2.5). The absorption spectrum and PL spectrum are shown in the figure 2.6. The first four excitation peaks were acquired based on previous reports [3] and the aforementioned Gaussian components fitting. Powder X-ray diffraction (XRD) patterns were collected using a Bruker D8 diffractometer with CuKα X-ray source, and shown in figure 2.7.

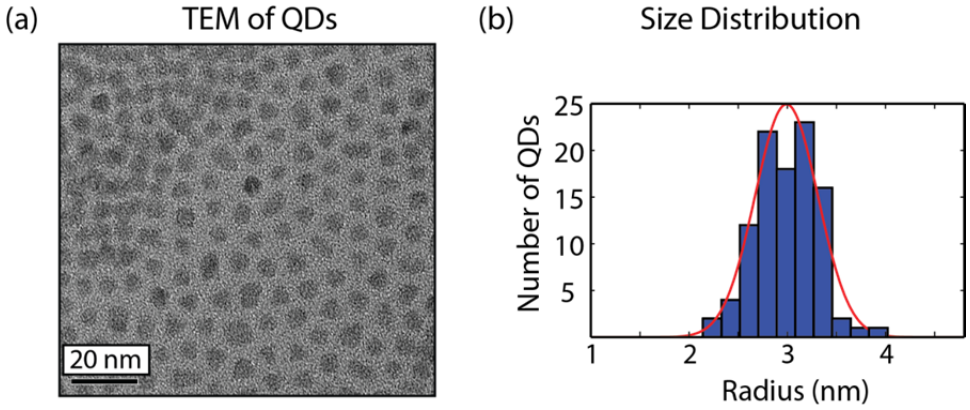

Figure 2.5 (a) TEM image of the larger zinc-blende CdSe quantum dots. (b) Size distribution derived from TEM image.

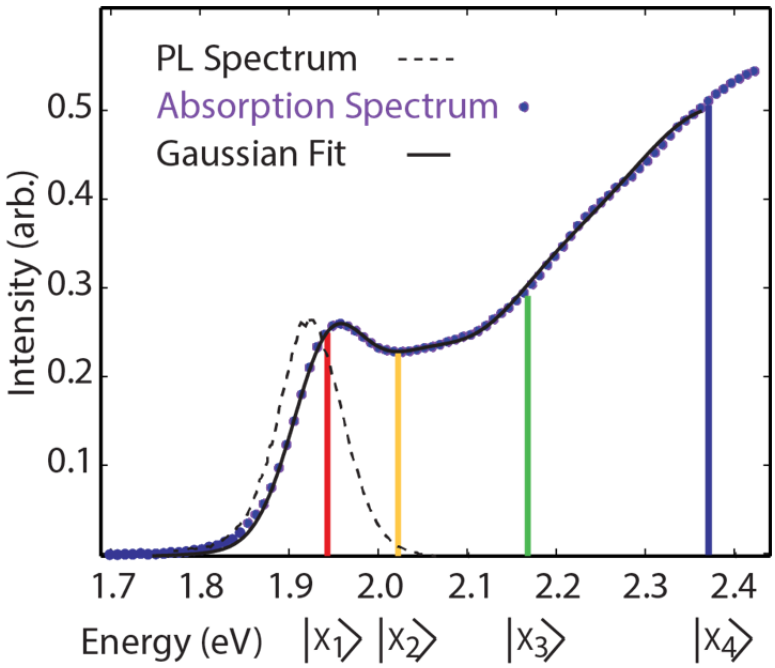

Figure 2.6 UV-Vis and PL spectrum of the zinc-blende CdSe quantum dots. The UV-Vis absorption spectrum was fit to four Gaussian components, and the center positions are indicated in orange, yellow, green, and blue vertical lines.

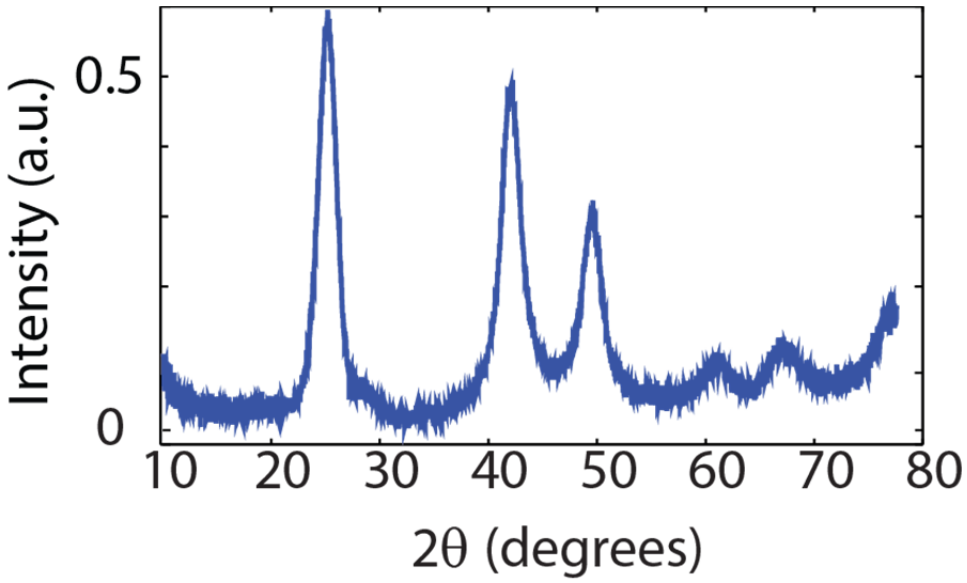

Figure 2.7 X-ray diffraction data showing zinc-blende crystallinity.

REFERENCES

[1] J. Li, Y. Wang, W. Guo, J. Keay, T. Mishima, M. Johnson, X. Peng, Large-scale synthesis of nearly monodisperse CdSe/CdS core/shell nanocrystals using air-stable reagents via successive ion layer adsorption and reaction, Journal of the American Chemical Society, 125 (2003) 12567-12575.

[2] C. Pu, J. Zhou, R. Lai, Y. Niu, W. Nan, X. Peng, Highly reactive, flexible yet green Se precursor for metal selenide nanocrystals: Se-octadecene suspension (Se-SUS), Nano Research, 6 (2013) 652-670.

[3] D. Norris, M. Bawendi, Measurement and assignment of the size-dependent optical spectrum in CdSe quantum dots, Physical Review B, 53 (1996) 16338-16346.

[4] L. Carbone, C. Nobile, M. De Giorgi, F. Sala, G. Morello, P. Pompa, M. Hytch, E. Snoeck, A. Fiore, I. Franchini, M. Nadasan, A. Silvestre, L. Chiodo, S. Kudera, R. Cingolani, R. Krahne, L. Manna, Synthesis and micrometer-scale assembly of colloidal CdSe/CdS nanorods prepared by a seeded growth approach, Nano Letters, 7 (2007) 2942-2950.

[5] D. Talapin, J. Nelson, E. Shevchenko, S. Aloni, B. Sadtler, A. Alivisatos, Seeded growth of highly luminescent CdSe/CdS nanoheterostructures with rod and tetrapod morphologies, Nano Letters, 7 (2007) 2951-2959.

[6] D. Battaglia, B. Blackman, X. Peng, Coupled and decoupled dual quantum systems in one semiconductor nanocrystal, Journal of the American Chemical Society, 127 (2005) 10889-10897.

[7] W. Yu, L. Qu, W. Guo, X. Peng, Experimental determination of the extinction coefficient of CdTe, CdSe, and CdS nanocrystals, Chemistry of Materials, 15 (2003) 2854-2860.

[8] O. Chen, X. Chen, Y. Yang, J. Lynch, H. Wu, J. Zhuang, Y. Cao, Synthesis of Metal-Selenide Nanocrystals Using Selenium Dioxide as the Selenium Precursor, Angewandte Chemie-International Edition, 47 (2008) 8638-8641.

3 Nonlinear Spectroscopies and Data Analysis

This chapter reviews the nonlinear spectroscopies that used for the experiments introduced in the next chapters, including two-dimensional electronic spectroscopy and pump-probe spectroscopy. The basic principles and optical setups are discussed. The data acquisition and analysis methods are also demonstrated.

3.1 The generation of laser pulses

A laser (light amplification by simulated emission of radiation) is a device that emits light through light amplification based on the stimulated emission of electronic radiation [1]. The scheme is shown in the figure 3.1. For stimulated emission to be the dominant process, the excited state population N_2 must be larger than the lower state population N_1. This phenomena of population inversion is accessed by pumping the gain medium.

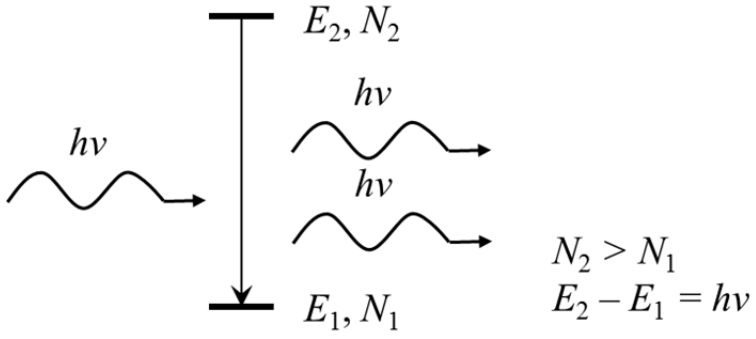

Figure 3.1 The diagram shows the population inversion. Stimulated emission dominates over absorption when light interacts with this gain medium.

In our setup, a diode-pumped Nd:YAG continuous wave (CW) laser is used to pump the Ti:Sapphire oscillator. After mode locked in the cavity, a pulse centered near 800 nm with a bandwidth of ~60 nm (FWHM) is generated. We used the commercial device (Micra, Coherent), to produce this ultrashort broadband laser pulse of about 500 mW power. Then the laser pulse is steered into the regenerative amplifier (Legend Elite, Coherent). First the pulse is stretched temporally to hundreds of picoseconds; then it is directed to seed the cavity in the regenerative amplifier. The Ti:Sapphire crystal in this cavity is pumped with a Nd:YLF laser at a power of 30 watts. After bouncing about 15 trips within the cavity, the seed pulse is amplified to ~3.6 watts. By controlling the voltage applied on two Pockels cells set in the cavity to either trap or eject the laser pulse, a 5 kHz pulse train is generated. These pulses are compressed by a grating before leaving the regen box, and we can get laser pulses (regen pulses) with a power of 2.8-3.3 W, 38 femtosecond duration, and 35 nm (FWHM) centered near 800 nm. The power stability of the laser pulses at this point is less than 0.2%.

3.2 Self-phase modulation and the white light generation

Self-phase modulation is a nonlinear optical effect during electronic field and matter interaction. In general, when apply an electric field (laser pulses in our experiment) onto a material, its refractive index changes, and is proportional to the square of the electric field. This induced refractive index will lead to a frequency shift of the spectrum.

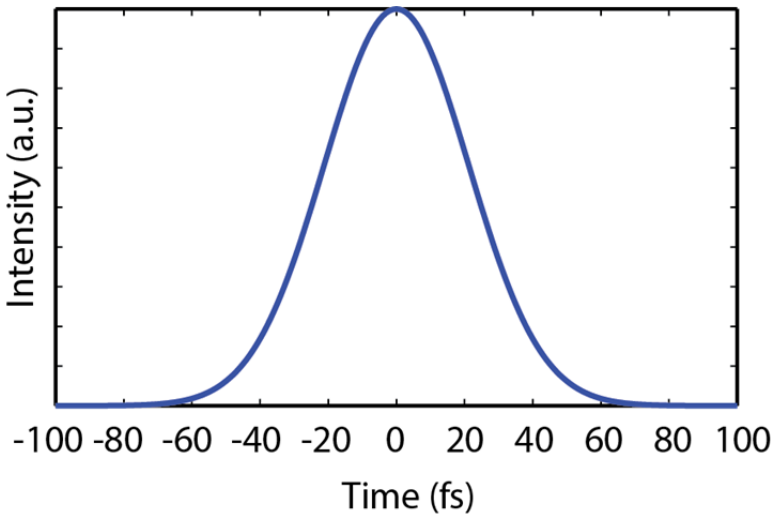

Figure 3.2 A Gasussian shape pulse of a pulse duration τ = 30fs.

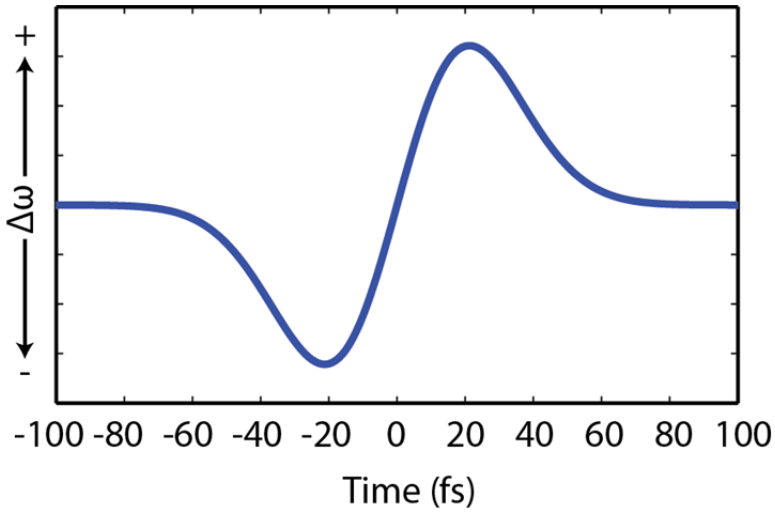

Figure 3.3 Instantaneous frequency changes of an initially unchirped pulse, due to self-phase modulation.

In a simple picture as shown in the figure 3.2, for a Gaussian shape pulse, the intensity is given by:

$$I(t) = I_0 e^{-t^2/\tau^2} \tag{3.1}$$

where I_0 is the amplitude of the pulse, and τ indicates the pulse duration. The induced refractive index is proportional to the square of the electric field:

$$n = n_0 + \Delta n = n_0 + kE^2 = n_0 + kI \tag{3.2}$$

where n_0 is the linear refractive index, and k is the second order nonlinearity. Combining equation (3.1) and (3.2), we will get

$$\frac{dn}{dt} = k\frac{dI}{dt} = kI_0\frac{d(e^{-t^2/\tau^2})}{dt} = kI_0(\frac{-2t}{\tau^2}\cdot e^{-t^2/\tau^2}) \tag{3.3}$$

The phase of the pulse then will change due to the induced refractive index:

$$\phi(t) = \omega_0 t - \vec{k}\cdot\vec{r} = \omega_0 t - \frac{2\pi}{\lambda_0}nL \tag{3.4}$$

where ω_0 is the carrier frequency of the pulse, λ_0 is the wavelength, and L is the distance that the pulse traveled. Then the time dependent instantaneous frequency can be deduced:

$$\omega(t) = \frac{d\phi(t)}{dt} = \omega_0 - \frac{2\pi}{\lambda_0}\cdot L\cdot\frac{dn}{dt} = \omega_0 - \frac{2\pi}{\lambda_0}\cdot L\cdot kI_0(-2t\cdot e^{-t^2/\tau^2}) \tag{3.5}$$

Using equation (3.3) and (3.5),

$$\omega(t) = \omega_0 + \frac{4\pi}{\lambda_0}\frac{LkI_0}{\tau^2}(t\cdot e^{-t^2/\tau^2}) \tag{3.6}$$

The equation (3.6) is plotted in the figure 3.3. We can tell that when t is positive (the pulse tail), the frequency will increase and lead to a blue shift; while when t is negative, the frequency will decrease and the wavelength will red shift. The frequency shift is also sensitive to length of the medium, the intensity of the pulse and the second order nonlinearity k.

In our experiment, we focused the aforementioned 800nm regen pulses into a pipe filled with argon gas. The length of 2.0 meters and pressure of 15 psi was selected to get desired wavelength. In addition, the power of the regen pulse (2.8 – 3.3 W) is also critical to generate white light.

Light redder than 700 nm is filtered by a hot mirror, producing a spectrum with FWHM from 480 to 680 nm, as shown in the figure 3.4 [2-6].

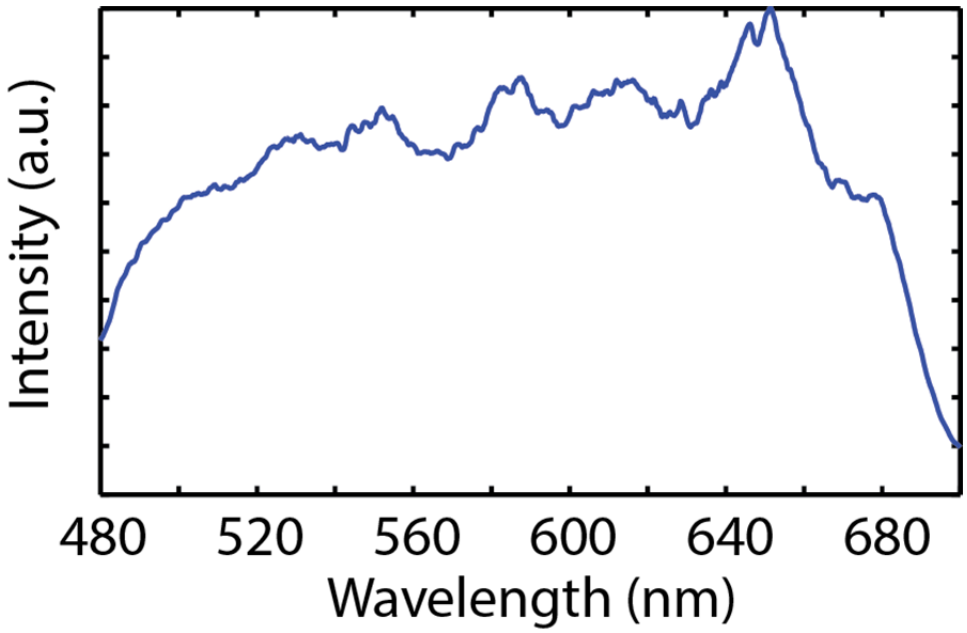

Figure 3.4 The broadband continuum white-light pulse measured after the hot mirror filter.

3.3 Two dimensional spectrometer and pump-probe spectrometer

The white light (power fluctuation is less than 1%) is then compressed using the Multiphoton Intrapulse Interference Phase Scan (MIIPS) method [7-9] and a spatial light modulator (Biophotonic Solutions, Inc.) is used to correct for dispersion. We compensated the white light pulses by optimizing the second harmonic generation (SHG) signal FWHM at the sample position using the MIIPS. The pulse duration was measured to be ~6 fs with the MIIPS and ~8-10 fs with the Transient Grating Frequency Resolved Optical Grating (TG-FROG), at the sample position. In the spectrometer, the pulse split into two beams by a beam splitter, and the time delay between them (waiting time *T*) is introduced using a retroreflector mounted on a translation stage (Aerotech). Then these two pulses are split again into four pulses, the time delay between

pulse 1 and pulse 2 (coherence time τ) is then controlled by a four mirror system with two translation stages. Then these four pulses are focused by a 15 degree off-axis silver parabolic mirror into a 100 μm spot at the sample position. The first three pulses interact with the sample, and generating a third-order response signal, which is emitted at the direction of the fourth pulse (local oscillator, LO). More details about the spectrometer will be discussed in the next chapter. The signal and LO are re-collimated by another 15 degree off-axis silver parabolic mirror, and focused into the camera (Newton, Andor) where it is frequency-resolved and heterodyne-detected.

In pump-probe experiment, the output pulse from MIIPS was guided into the pump-probe setup and compressed separately for the pump-probe measurement. The 5.0 kHz pump beam was chopped at 2.5 kHz, so that the pump-probe and probe-only spectra were collected alternatively on a high-speed line scan camera (Horiba). Time delay between the pump and probe pulses is controlled by a translational stage that adjusts the path-length of the pump pulse to the sample position. The pump-probe data was acquired for all time delays matching the waiting times of the 2DES measurement. The third-order signal then emits at the direction of the probe pulse, and heterodyned with the probe pulse.

3.4 Data acquisition and analysis in 2DES

The camera was calibrated using Neon or Argon lamps. Via fitting the peak positions to their atomic spectra, it becomes possible to link pixels numbers to wavelengths. Then all three translation stages were calibrated using spectral interferometry [10]: we typically place a thin glass slide with finger prints on, to increase the scatter signal, and get a nice interferogram of two

pulses. By scanning one pulse relative to another one, we can build a plot of time-delay versus the distance that translation stage moved. Fitting this plot gives the calibration constant for the translation stage that moved. The timing zero (pulse 1, 2, 3 are temporally overlapped) was reached using TG-FROG [11]. The LO was set about 1200 fs from the beam 3, and attenuated of 4-5 orders to match the intensity of the third-order signal. For each waiting time T, we either scan the pulse 1 ahead of pulse 2, or scan the pulse 2 ahead. The pulse sequence is shown in the figure 3.5. For each specific τ and T, we control the shutter to block and unblock the pulse 3 to record both the signal with all four pulses I_{1234} and that without pulse 3, I_{124}. After finishing scan τ, the signal with only pulse 3 and LO in, I_{34} is recorded by the camera, for each specific waiting time T. Finally, the spectrum of LO, I_4 is also recorded.

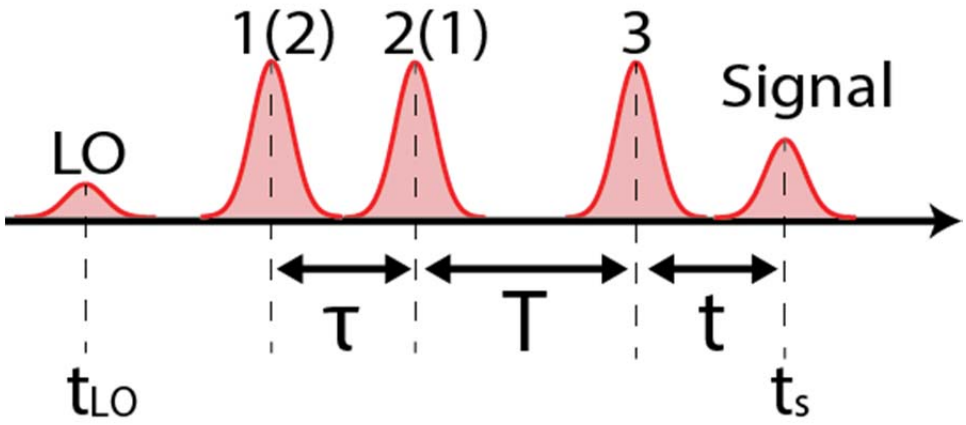

Figure 3.5 Pulse sequence in 2DES. The LO signal arrives first. Then either pulse 1 comes early (rephasing), or the pulse 2 comes early (nonrephasing). The time delay between the first and second pulses is the coherence time τ. The time delay between the second and third pulses is the waiting time T. The third-order signal is emitted after pulse 3, in a delay of the rephasing time t.

The scatter subtraction was illustrated by Brixner [10].

$$I_{1234} = \left| E_1 + E_2 + E_3 + E_{LO} + E_{sig} \right|^2 \tag{3.7}$$

$$I_{124} = \left|E_1 + E_2 + E_{LO}\right|^2 \tag{3.8}$$

$$I_{34} = \left|E_3 + E_{LO}\right|^2 \tag{3.9}$$

$$I_4 = \left|E_{LO}\right|^2 \tag{3.10}$$

Combining equation (3.7)-(3.10), we will get

$$I_{1234} - I_{124} - I_{34} + I_4 = E_1 E_3^* + E_2 E_3^* + (E_1 + E_2 + E_3 + E_{LO}) \cdot E_{sig}^* + E_{sig} E_{sig}^* + c.c. \tag{3.11}$$

The I_{1234} is shown in the figure 3.6(a), and the subtracted signal in equation (3.11) is shown in the figure 3.6(b). However, since the rephasing axis is linearly spaced in wavelength, Fourier interpolation along this axis is processed to make the signal linearly dispersed with frequency (λ_t to ω_t). The 2D plot after this Fourier interpolation is shown in the figure 3.6(c). We then Fourier transfer along the rephasing axis (ω_t to t) (figure 3.6(d)), and apply a window function to apodize the signal and eliminate both residual scatter and the homodyne signals. For equation (3.11), only terms at the selected delay time t_s - t_{LO} (figure 3.5) will be kept, so the data is simplified to

$$I = E_4^* \cdot E_{sig} \tag{3.12}$$

which is shown in in the figure 3.6(e). Finally, Fourier transfer over both dimensions ((τ,t) to (ω_τ,,ω_t)), the 2D spectrum in frequency-frequency domain, as shown in figure 3.6(f)

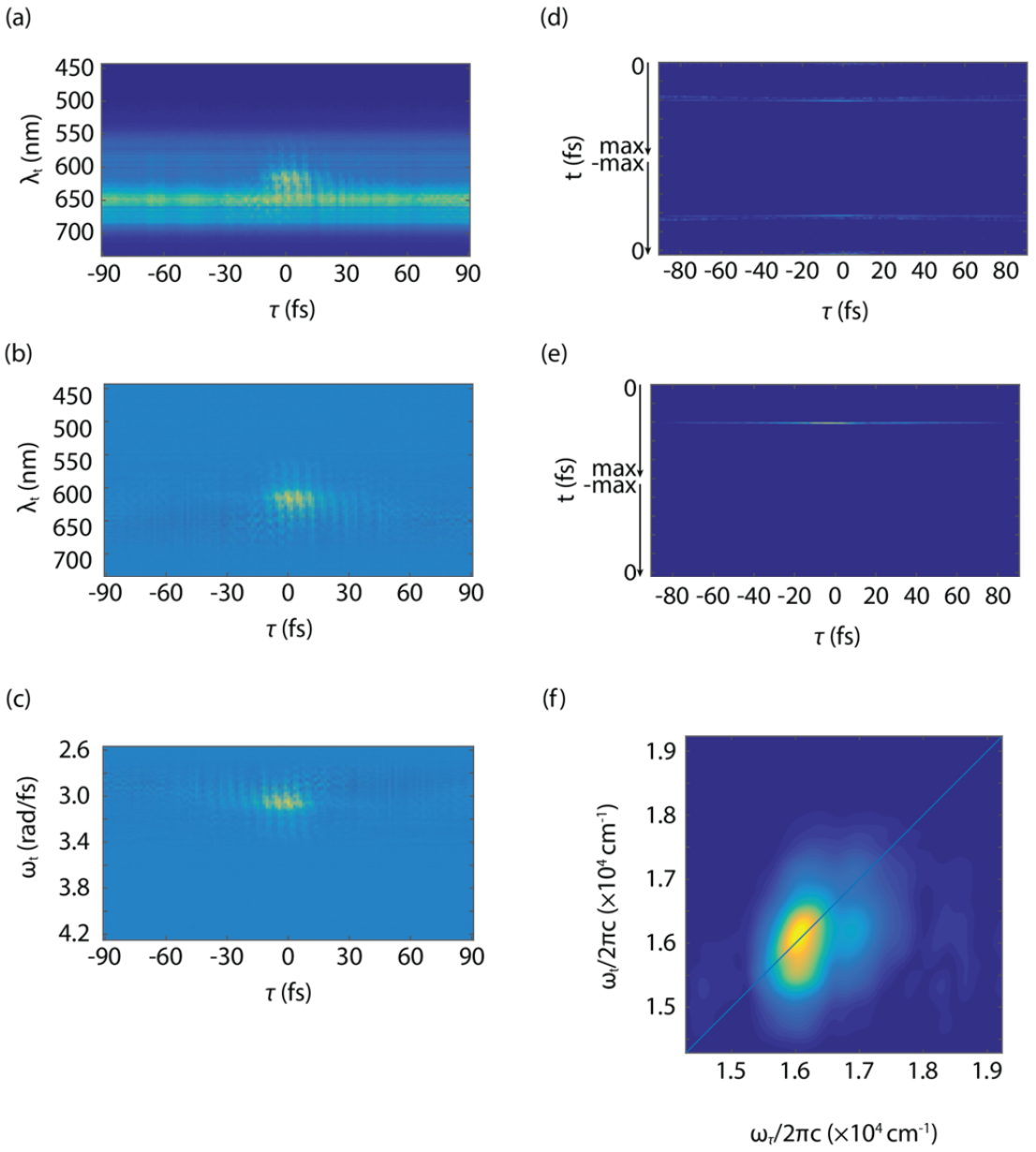

Figure 3.6 Data analysis for 2DES. (a) Raw signal with all four beams in, for a specific waiting time T. The coherence time was scanned from 90 to -90 fs, in steps of 1.5 fs. (b) The signal after scatter subtraction. (c) The signal after interpolation, linearly spaced in frequency domain for the rephasing axis. (d) Time-Time plot. (e) Time-Time plot after applied the window function. (f) 2DES Spectrum in frequency-frequency domain.

3.5 Data acquisition and analysis for pump-probe experiment

In pump-probe experiment, the pump-probe and probe-only spectra were collected alternatively for each waiting time *T*. We average these signals of 3-10 shots to minimize the fluctuation. Similar to 2DES data analysis:

$$I_{pp} = \left| E_{pump} + E_{probe} + E_{sig} \right|^2 \tag{3.13}$$

$$I_{p} = \left| E_{probe} \right|^2 \tag{3.14}$$

Where E_{pump} is the scatter from the pump pulse, and E_{probe} is the electronic field of probe pulse

By doing subtraction, we will get

$$I_{pp} - I_{p} = \left| E_{pump} \right|^2 + \left| E_{sig} \right|^2 + \left[E_{pump} E_{sig}^{*} + E_{probe} E_{sig}^{*} + E_{pump} E_{probe}^{*} + c.c. \right] \tag{3.15}$$

which is shown in the figure 3.7(a). After interpolated to be linearly spaced in frequency domain, we Fourier transform over camera frequency and get figure 3.7(b). We can get the peak positions of each individual interferogram of $E_{\text{pump}}E_{\text{probe}}^{*}$ at different waiting times. Fitting this movement of peak position, we can get the correct waiting time axis (inset of figure 3.7 (b)). Applying a window centered at time zero gives

$$\left| E_{pump} \right|^2 + \left| E_{sig} \right|^2 + \left[E_{probe} E_{sig}^{*} + c.c. \right] \tag{3.16}$$

The first term can be removed by subtraction of the background at negative waiting time, where only the first term exists in equation (3.16). The second term can be neglected since it is much weaker than the heterodyne. After apply another window in ω_t domain to remove optical frequency, and divided by E_{probe}, the pump-probe spectrum is shown in the figure 3.7(c).

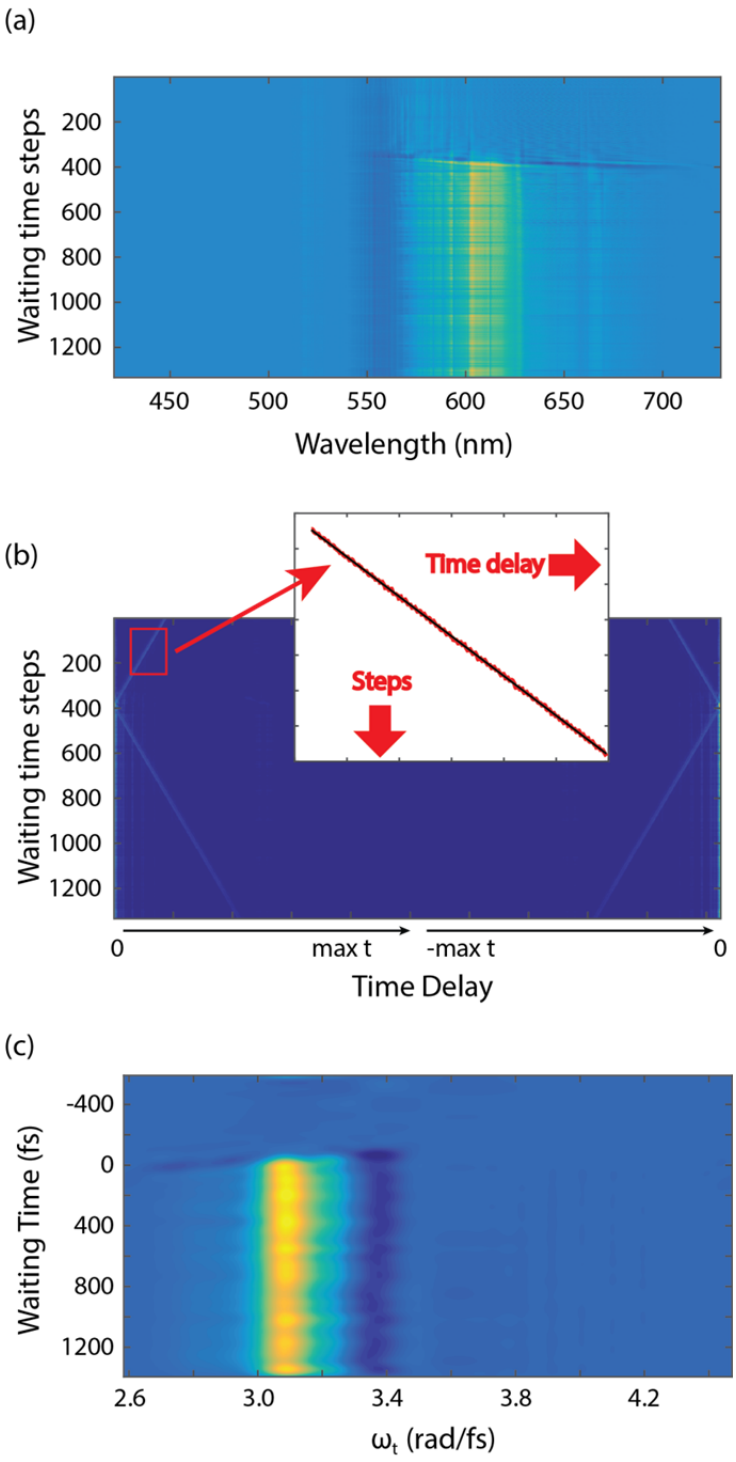

Figure 3.7 Data process for pump-probe experiment. (a) The raw data after subtraction. (b) Interpolated the wavelength to frequency domain, and Fourier transform to get the scatter. By fitting the peak position of the scatter, we can get the actual time delay between pump and probe (waiting time). (c) Final pump-probe spectrum after windowing and subtraction.

3.6 Phasing 2D spectrum

After get the 2D and pump-probe spectra, the final step is to determine the absolute phase of the 2DES spectrum, which can be recovered by fitting the 2D spectrum to pump-probe signal. We used the projection slice theorem as shown here:

$$PP(T,\omega_t) = \mathrm{Re}\left\{ A\int_{-\infty}^{\infty} S_{2D}(\omega_\tau, T, \omega_t)\exp\left(i\varphi + i(\omega_t-\omega_0)t_c + i(\omega_t-\omega_0)^2 t_q^2 + i(\omega_\tau-\omega_0)\tau_c\right)d\omega_\tau \right\} \quad (3.16)$$

where φ is an overall constant phase correction, t_c and τ_c correct for timing between beam 3 and LO and errors in timing between beams 1 and 2 respectively, and t_q corrects the quadratic nonlinear dispersion arising from neutral density filter in the local oscillator beam. A example of the fitting result is shown in the figure 3.8.

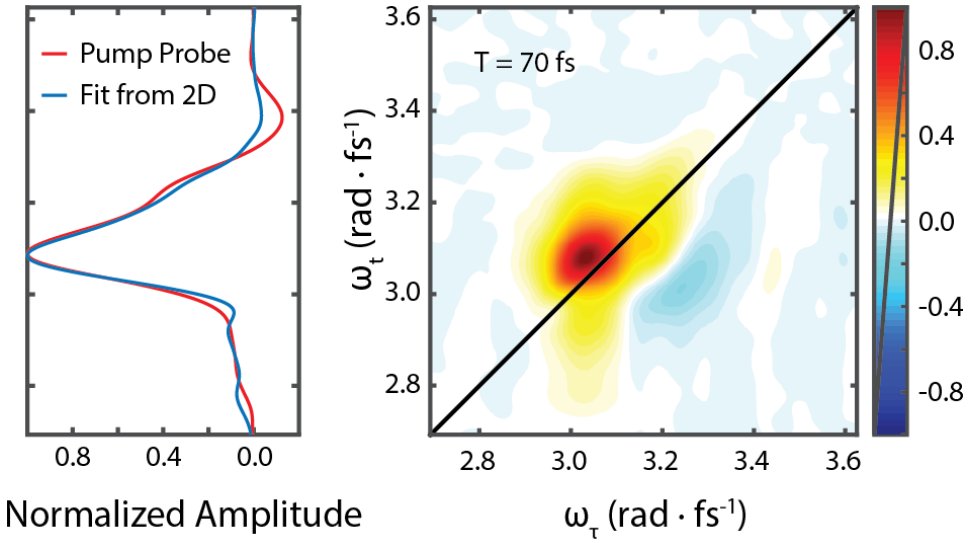

Figure 3.8 The fitting result when phasing 2D spectrum using pump-probe data.

After phasing, the real (absorptive) and imaginary (dispersive) components of 2DES spectrum are separated. Figure 3.8 shows one example of real value of 2DES spectrum. An identical set of phase correction constant is applied on all 2DES spectra at different waiting times.

All phased 2DES spectra are stacked into a cube, to provide more information of quantum coherence, relaxations or spectral lineshape.

REFERENCES

[1] R.G. Gould, The LASER, Light Amplification by Stimulated Emission of Radiation *The Ann Arbor Conference on Optical Pumping*, *1959*, pp. 128.

[2] M. Nisoli, S. DeSilvestri, O. Svelto, Generation of high energy 10 fs pulses by a new pulse compression technique, Appl Phys Lett, 68 (1996) 2793-2795.

[3] M. Nisoli, G. Sansone, S. Stagira, C. Vozzi, S. De Silvestri, O. Svelto, Ultra-broadband continuum generation by hollow-fiber cascading, Appl Phys B-Lasers O, 75 (2002) 601-604.

[4] G. Steinmeyer, G. Stibenz, Generation of sub-4-fs pulses via compression of a white-light continuum using only chirped mirrors, Appl Phys B-Lasers O, 82 (2006) 175-181.

[5] H. Wang, Y. Wu, C. Li, H. Mashiko, S. Gilbertson, Z. Chang, Generation of 0.5 mJ, few-cycle laser pulses by an adaptive phase modulator, Opt Express, 16 (2008) 14448-14455.

[6] K. Yamane, Z. Zhang, K. Oka, R. Morita, M. Yamashita, A. Suguro, Optical pulse compression to 3.4 fs in the monocycle region by feedback phase compensation, Opt Lett, 28 (2003) 2258-2260.

[7] B. Xu, Y. Coello, V. Lozovoy, D. Harris, M. Dantus, Pulse shaping of octave spanning femtosecond laser pulses, Opt Express, 14 (2006) 10939-10944.

[8] B. Xu, J. Gunn, J. Dela Cruz, V. Lozovoy, M. Dantus, Quantitative investigation of the multiphoton intrapulse interference phase scan method for simultaneous phase measurement and compensation of femtosecond laser pulses, Journal of the Optical Society of America B-Optical Physics, 23 (2006) 750-759.

[9] D.B. Turner, K.W. Stone, K. Gundogdu, K.A. Nelson, Invited Article: The coherent optical laser beam recombination technique (COLBERT) spectrometer: Coherent multidimensional spectroscopy made easier, Rev Sci Instrum, 82 (2011).

[10] T. Brixner, T. Mancal, I. Stiopkin, G. Fleming, Phase-stabilized two-dimensional electronic spectroscopy, Journal of Chemical Physics, 121 (2004) 4221-4236.

[11] J. Sweetser, D. Fittinghoff, R. Trebino, Transient-grating frequency-resolved optical gating, Optics Letters, 22 (1997) 519-521.

4 Dispersion-Free Two Dimensional Electronic Spectrometer

Electronic dynamics span broad energy scales with ultrafast time constants in the condensed phase. Two-dimensional electronic spectroscopy permits the study of these dynamics with simultaneous resolution in both frequency and time. In practice, this technique is sensitive to changes in nonlinear dispersion in the laser pulses as time delays are varied during the experiment. In this chapter, we developed a two-dimensional spectrometer which uses broadband continuum generated in argon as the light source. We demonstrated all-reflective interferometric delays using angled stages, in the phase-sensitive optical experiments. Upon selecting a ~180 nm window of the available bandwidth at ~10 fs compression, we probed the nonlinear response of broadly absorbing CdSe quantum dots and electronic transitions of Chlorophyll *a*.

4.1 The timing control in 2DES

We exploit a simple method of obtaining precision time delays using reflective optics and angled translational stages here. This method allows us to probe materials with ground-state and transient spectral features spanning several hundred nanometers, while limiting nonlinear dispersion.

The details of 2DES have been discussed extensively previously [1-5], and introduced in the chapter 3. Briefly, a sequence of three ultrafast laser pulses interact with the sample with precisely controlled time delays. The first and second pulses interact with a time separation τ (coherence time), during which the system evolves in an optical coherence between the ground and excited states. After the second interaction, the system undergoes evolution in the excited or ground state manifolds for a waiting time T, then a third pulse puts the system into a second

optical coherence. We then heterodyne the signal emitted in the phase-matched direction ($-\boldsymbol{k}_1+\boldsymbol{k}_2+\boldsymbol{k}_3$), with an attenuated local oscillator (LO) pulse and collect data in the frequency domain using a CCD spectrometer. Interchange between pulses 1 and 2 allows collection of rephasing and non-rephasing spectra which, taken together, can be phased to generate absorptive or dispersive 2D spectra. Generation of phased 2DES spectra requires optical phase stability between the first two interactions and minimal temporal dispersion among the pulses [6, 7].

Several methods have been used to implement the requisite interferometric time delays in 2DES. Timings can be controlled using retroreflectors mounted on sinusoidal encoded or piezoelectric motor stages which move parallel to the direction of beam propagation with control of approximately 6673 fs/mm [8-10]. The accuracy can be further improved using active phase stabilization [11]. Delays can also be implemented with more precise control (<50 fs/mm) using paired, angled glass wedges, effectively "gearing" the delay [3, 4]. The delay between pulses 1 and 2 can also be encoded along a spatial dimension, where multiple time delays are directly imaged on a camera in a single experiment [12, 13]. Moreover, delays can be set using spatial light or acousto-optic modulators [14-17]. Finally, the Soleil-Babinet compensator has recently been used for generating a time delay between two pulses [18]. In this chapter, we seek fine temporal resolution across a wide bandwidth without changes in temporal dispersion, therefore we avoid transmissive optics. As a result, we have designed a simple system to control the time delay with high resolution, while using all reflective optics. Using this method, we can utilize continuum broadband laser without nonlinear dispersion introduced by differential amounts of glass. Incorporating supercontinuum light sources in 2DES is now allowing access to broader spectral regions and even ultraviolet 2DES [19-24].

4.2 Experimental design

The experimental apparatus is shown in figure 4.1. The regen pulse and white light generation were discussed in the last chapter. Briefly, The 800 nm output of a Coherent Micra Ti:Sapphire oscillator was amplified in a Coherent Legend Elite regenerative amplifier to produce a 5 kHz, 4 W, 38 fs FWHM pulse train centered at 800 nm. By focusing the pulse into a 2 m tube filled with 2 atm of argon gas, ultra-broadband pulses spanning from 450 to 900 nm were generated [25-29]. Using a dichroic mirror (replaced with hot mirror later), light redder than 700 nm is attenuated and the portion spanning 525 nm to 700 nm (shown in figure 4.2) is shaped and then compressed using the Multiphoton Intrapulse Interference Phase Scan (MIIPS; Biophotonic Solutions, Inc.) method [30-32]. We compensated for dispersion by optimizing the second harmonic generation (SHG) signal FWHM at the sample position using the MIIPS. To further validate the instrument, we performed Transient Grating Frequency-Resolved Optical Grating (TG-FROG) in neat methanol to characterize the temporal behavior (shown in figure 4.3) [33-35]. The pulse duration was measured with MIIPS at the sample position to be ~8 fs (as shown in the inset of figure 4.3(c)), with <5% deviation from the transform limit.

Continuum pulses were split using a set of two beam splitters. The first beamsplitter separates beams 1 and 2 from beams 3 and LO, and then beams 1 and 2 are delayed using a retroreflector mounted to a motorized linear stage (Aerotech) to set the waiting time. These vertically separated beams are split again using a second beam splitter to generate four equal pulses in a boxcar geometry with 12 mm separation. Each beam propagates through identical amounts of optical glass, including neutral density and corresponding compensation plates. The coherence time was controlled by the purely reflective delay system. Our approach translates a flat mirror aligned to reflect the level incoming beam upwards at a small angle. The mirror is

translated nearly perpendicular (~0.3 degrees horizontally from the plane normal to beam propagation) to the incident beam path. This implementation of a purely reflective delay stage differs from the four quadrant mirror introduced by Zhang et.al [10]. In our implementation, as the position of the incident beam moves along the translating mirror, the optical path length changes slightly resulting in controllable delay and negligible translation of the outgoing beam.

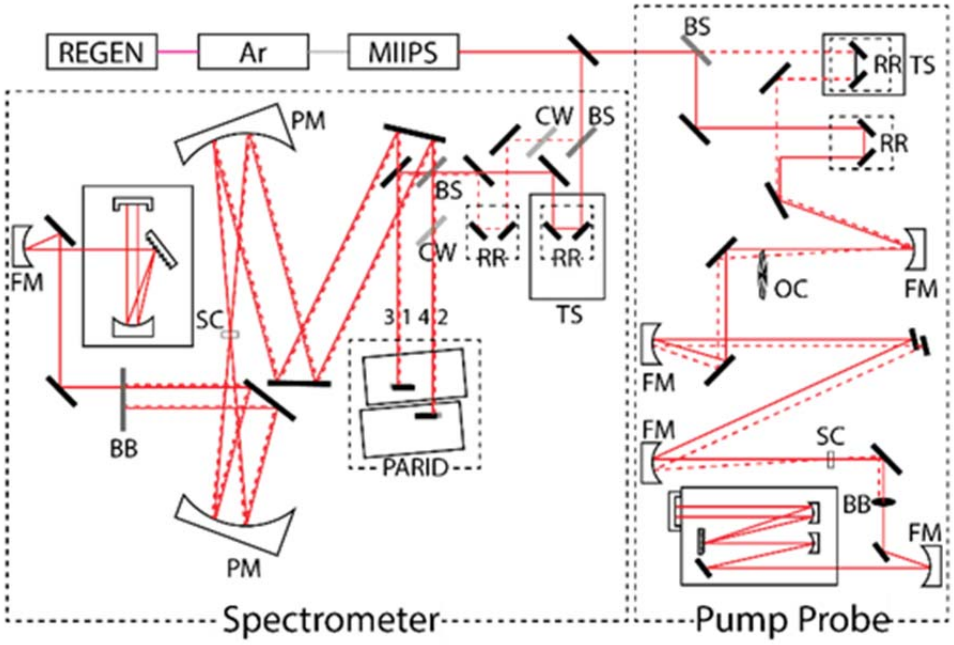

Figure 4.1 Experimental Implementation for Continuum Two-Dimensional Electronic Spectroscopy (C-2DES): An ultrafast pulse is split into four pulses using beamsplitters (BS); compensating windows (CW) are introduced in each beam to ensure all beams pass through the same amount of glass. A retro-reflector (RR) mounted on a translation stage (TS) introduces the waiting time delay, T. The all reflective interferometric delay system (ARID) controls the coherence time τ by translating mirrors nearly perpendicular to the incoming beams. An off-axis parabolic mirror (PM) focuses the four beams on the sample cell (SC). The signal field and LO pass through a beam block (BB) and are imaged on a CCD detector. In the accompanying pump-probe experiment, we introduce an optical chopper (OC) to modulate the pump beam.

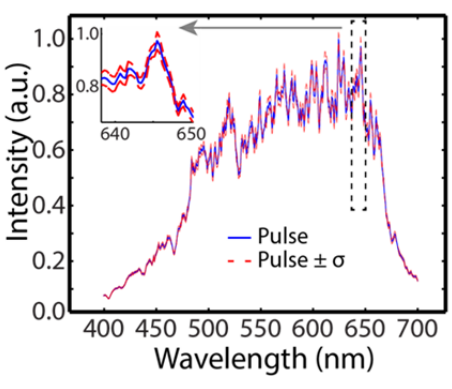

Figure 4.2 Stability of supercontinuum source: The white light spectrum from the supercontinuum source before spectral shaping in the Biophotonics MIIPS system is shown above (blue, solid). To obtain this spectrum, the supercontinuum is filtered by a dichroic mirror which removes light above 700 nm. The wavelength-dependent fluctuations (red, dashed, ±1σ) measured every 5 seconds over a 24 min period are ~0.5% across the entire spectrum.

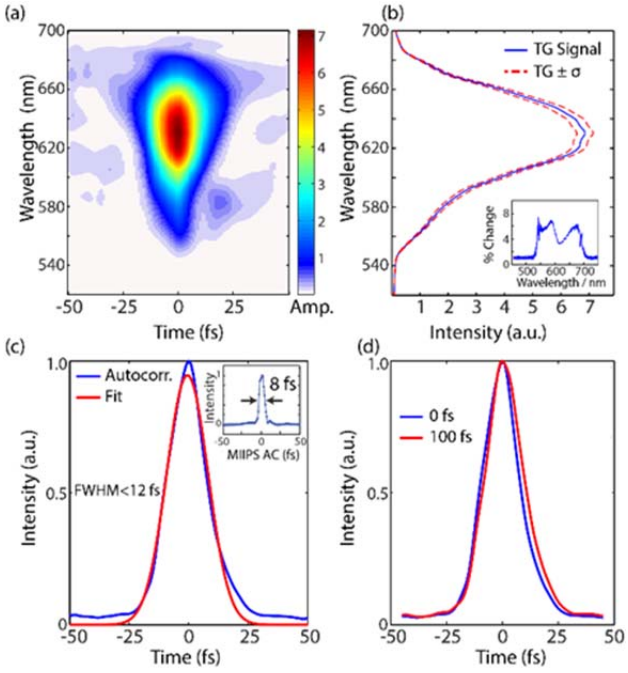

Figure 4.3 (a) Representative Transient Grating Frequency-Resolved Optical Gating (TG-FROG) measurements. (b) The TG signal and the wavelength-dependent standard deviation (1σ) when all three pulses are overlapped indicate approximately 0.5% third-order signal stability. The inset shows flat, wavelength-dependent fluctuations. (c) Shown is the sum the TG trace and the fit to a Gaussian function, from which we derive an autocorrelative width of 12 fs. The inset shows the corresponding MIIPS trace with 8 fs width (FWHM). (d) Two autocorrelation traces taken at different delay configurations show that intensity does not change (less than 1% change) when all stages are translated 100 fs (data not individually normalized).

The pulses are then focused to a 100 μm diameter spot on the sample with a 15º off-axis parabolic gold mirror (replaced with silver mirror later) of 45 cm effective focal length. After recollimation by another parabolic mirror and selection of the phase-matched signal ($-\boldsymbol{k}_1+\boldsymbol{k}_2+\boldsymbol{k}_3$) using a mask, we focus the signal and LO into a 0.3 m spectrometer (Shamrock, Andor) and camera (Newton, Andor) where it is frequency-resolved and heterodyne-detected. The bandwidth and focal properties satisfy constraints for spatial conditions laid out in previous theoretical studies [36]. Spatial beam translation caused from this delay strategy is measured and characterized below.

We use separately collected transient absorption spectra to phase each two-dimensional spectrum [4, 37-39]. The power is attenuated to achieve a pump pulse of 40-70 nJ/pulse and a probe pulse power of 0.44 nJ. Results are qualitatively consistent with previous broadband pump-probe work performed on these systems [40-42]. A standard delay stage (Aerotech) alters the path length of the pump pulse relative to the probe to generate the temporal delay. An MC2000 optical chopper (Thorlabs, Inc.) synchronized to the regenerative amplifier output modulates the pump pulse at half the laser repetition rate, resulting in every other shot generating a probe or pump-probe spectrum. The pump and probe beams are focused to an approximately 100 μm spot in the sample. The probe and pump-probe signals are then focused into a MicroHR spectrometer (Horiba Scientific). The spectrally resolved probe/pump-probe signals are recorded using a high-speed, line scan Spyder3 camera (Teledyne Dalsa) at 5 kHz synchronized to the output of the regenerative amplifier. The pump-probe experimental setup is also shown in the figure 4.1.

4.3 Characterizations of the spectrometer

In figure 4.2, we show power stability of our white light spectrum acquired over 25 minutes, demonstrating fluctuations of less than 0.5% across the visible range. The phase stability of the instrument was measured by recording a series of interferograms between beams 3 and LO. Using the method described by Prokhorenko[43], we measure phase stability between each of the beams of λ/75 at 800 nm over 2.5 hours (figure 4.4), compared with λ/100 which was taken using the third-order signal and local oscillator[8] in a passively phase-stabilized configuration[4]. One representative interferogram is shown in figure 4.5(a), illustrating the broadband interferogram and relative phase consistency between each beam. We use this interferogram to measure the frequency-dependent dispersion profiles at the sample. To verify that each beam propagates through identical glass, we apply a moving window function Fourier transform across the wavelength dimension, which apodizes the interferogram. In the time-domain, we map the time delay for each wavelength component (figure 4.5(b)). A flat profile indicates that all frequencies have identical phase profiles at the sample position. We repeated this method for all pulse pairs to ensure compensating windows and neutral density filters are precisely matched.

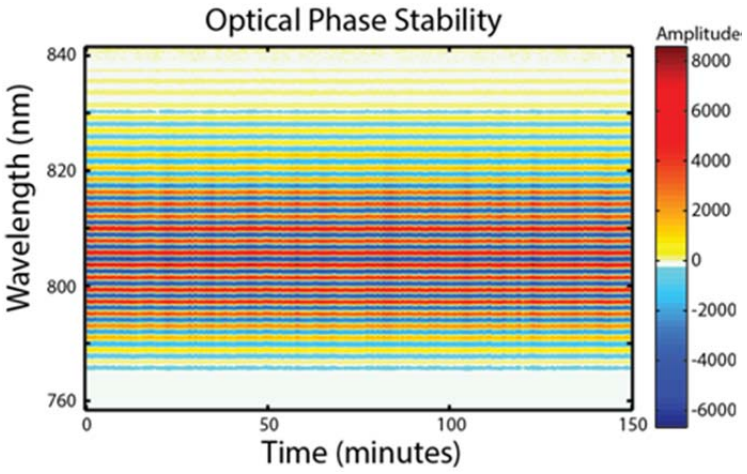

Figure 4.4 The optical phase stability between beams 3 and 4, measured every 45 seconds over 150 minutes, using the 800 nm pulse from the regenerative amplifier. This data illustrates the mechanical phase stability of the apparatus.

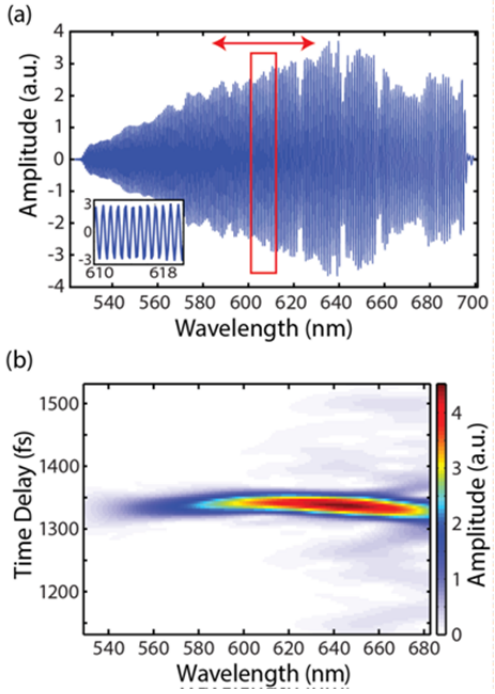

Figure 4.5 Characterization of compensating glass. (a) The interferogram of pulse 3 and LO after spectral filtering through the MIIPS compression system. The red box indicates the moving window function over which the Fourier transform is applied to generate the spectrogram below; (b) To illustrate relative dispersive characteristics between pulses, we move the window function shown in (a), to show the time domain signal across different wavelengths. This measure illustrates the relative spectral coherence of the pulse, indicating propagation through similar amounts of glass.

We have designed our reflective delay method to delay each beam while maintaining relative nonlinear dispersive profiles. Each beam reflects off an independent mirror which sets its time delay. Instead of moving mirrors along direction of beam propagation (as with a retroreflector), we mount the mirrors that set the coherence time on two identical translation stages which move at a small, horizontal angle θ relative to the plane normal to beam propagation. By setting the angle, we improve the resolution of the coherence time delay relative to retroreflectors by a factor of $1/\sin(\theta)$, from 6673 fs/mm to ~35 fs/mm (θ~0.3º). Furthermore, by increasing θ, we may lower the precision of time control, but be able to access a larger temporal range, which is necessary to scan long lived coherences (such as those accessed by systems with narrow lineshapes, like quantum wells and gas vapors). In figure 4.6, we show that this delay can be reliably scanned to generate time delays with 0.25 fs precision using a continuum source. Surface flatness of our optics is specified as $\lambda/10$ at 633nm, which yields a small error in calibration (~0.2 fs). We have extended Prokhorenko et al's method to extract phase stability using the timing extracted in figure 4.5, and shows that the stability during scan (including contributions from vibrations, mirror flatness, stage dither etc) of better than $\lambda/35$ (figure 4.7). We believe that the precision of our current system is sensitive to surface flatness. Nonetheless, this apparatus yields delays and precision similar to previous passively phase-stabilized techniques, wherein a pair of parallel glass wedges was used to control time delays [12, 44]. Each beam travels through different amount of glass to generate a temporal delay (< 50 fs/mm for 1 degree glass wedges) which provides excellent phase-stability but induces nonlinear, wavelength-dependent delays, leading to distinct chirp for each beam, which can lead to distorted lineshapes and false cross

peaks in two-dimensional spectra [45]. The distortion is even more significant when using ultra-broadband white light. For instance, when setting a 200 fs pulse delay using the wedge method, the red edge (700nm) would be 2.4 fs ahead of blue edge (520nm). Therefore, all reflective delay methods provide an avenue to explore longer coherence times, without introducing this nonlinear dispersion. We perform an autocorrelation with a pulse width of typically 10-12 fs, similar to the 8 fs measured by MIIPS. The slight discrepancy may relate to the three pulse nature of the TG measurement and coherent nuclear response of the blank solvent [46]. All colors appear well compressed and the TG shows a flat, nearly symmetric profile.

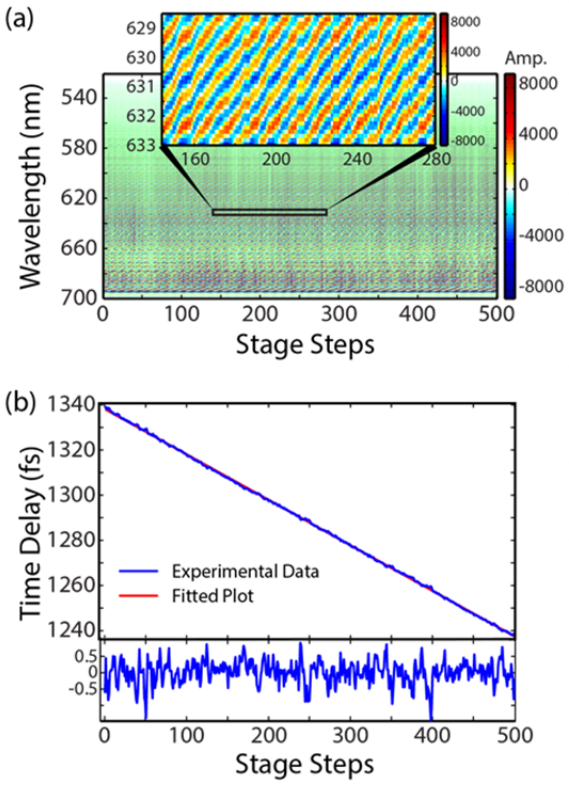

Figure 4.6 The interferogram between pulse 2 and LO when scanning pulse 2. The magnified portion indicates the interferometric detail of a representative smaller region. (b) Plot of the measured time delay between pulse 2 and LO at each step as measured by spectral interferometry from the data shown above (blue line). The red line shows the fit to a linear function. We plot the residual below. The standard deviation is ~0.30 fs/step which is approximately the Fourier limited resolution given the bandwidth of our laser pulse.

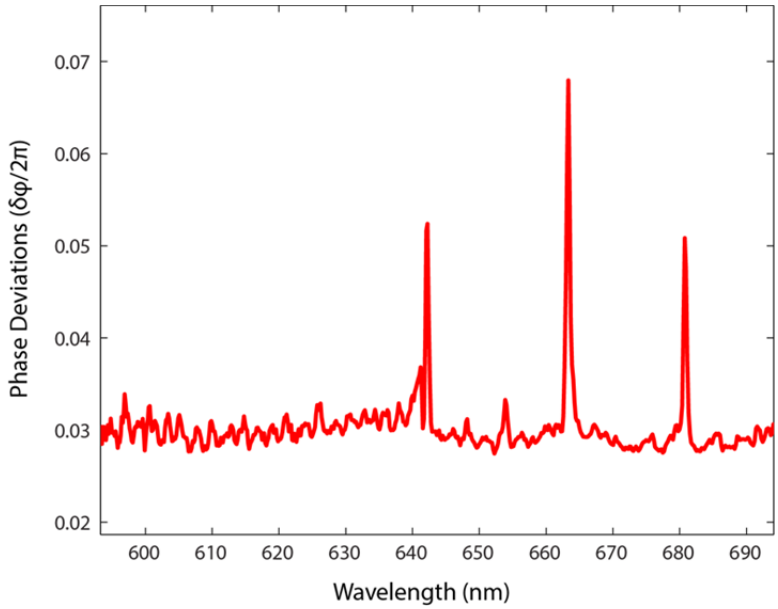

Figure 4.7 Phase stability characterization using the interferogram between pulse 2 and LO when scanning pulse 2. It shows that the phase stability is ~0.03 (λ/30) from 600 to 690 nm. We borrowed the method from Prokhorenko [43], and used the timing extracted in figure 4.5 (linearly chanced during scan) to obtain the actual phase. We calculated the standard deviation of the monitored actual phase for each different wavelength across the whole scan and plotted it in this figure.

This reflective delay method relies on angled stages and optical flats to generate precise time delays. To separate incoming and outgoing beams, we angle each optic upward approximately 3.5 degree with respect to the table top (see figure 4.8(a)), which results in a small vertical displacement during delay. In our implementation, a 100 fs delay yields a positional deviation of ~1μm at the sample position. In figure 4.3(d), we show a comparison between the original TG signal, and one in which beams 1 and 2 are delayed by 100 fs using all reflective delay system, while beam 3 is delayed using a mounted retroreflector that travels parallel to beam propagation. They show nearly identical response, illustrating minimal undesired side effects from adjusting the time delay.

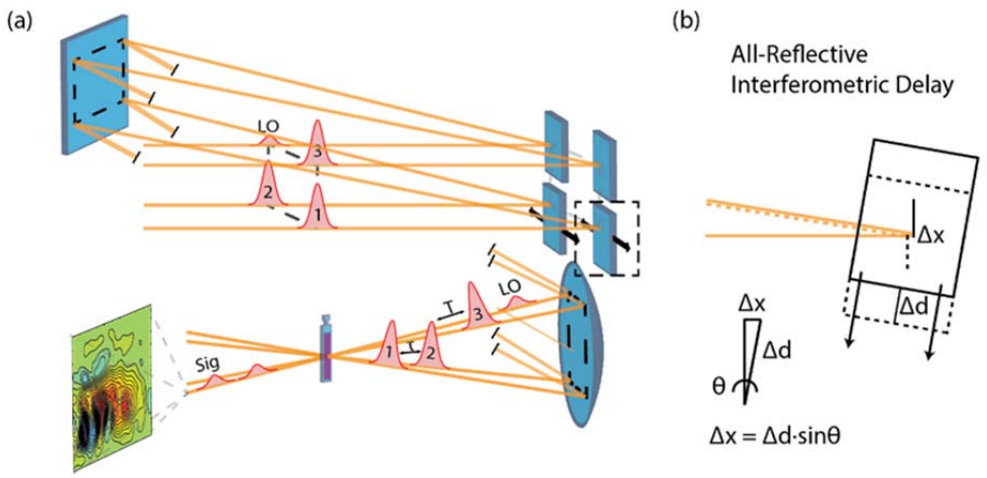

Figure 4.8 (a) Three-dimensional representation of the apparatus. The coherence time is introduced and changed using reflective optics. (b) A detail of the coherence time control with angled stages. This design shows that for a parallel input, fine control can be achieved by propagating the stage at a very small angle (typically 0.3º).

4.4 Fundamental applications of Dispersion-free continuum 2DES

We probe two different broadly absorbing systems, CdSe QDs in toluene and Chl*a* in methanol at 21 ºC. QD electronic structure and charge-carrier dynamics have been comprehensively reviewed in chapter 1. Briefly, quantum dots have discrete electronic states at and near the band-edge, which contribute to their optical nonlinear response. This electronic structure results in positive (stimulated emission/ground state bleaching) and negative (excited state absorption) signatures which can be probed to follow the electronic dynamics and the binding energy of biexcitons [47-51]. Previous two-dimensional spectroscopy on QDs primarily focused on the band-edge exciton or the first two excitons, which are primarily associated with the lowest lying excited electronic state [52-54]. Recent work, however, has shown that the nonlinear response varies depending on which state is initially excited, with the largest difference occurring upon initial excitation into the 1P(e) higher lying electron manifold [40, 55]. In figure

4.9(a), we show a two-dimensional spectrum (combined non-rephasing and rephasing) of a relatively polydisperse sample of quantum dots (10% radial inhomogeneity). We observe significant differences in the nonlinear response depending on excitation energy, both in the position and sign of peaks. The ability to resolve frequencies of responses domains enables us to probe detailed electronic dynamics despite the inhomogeneity of the ensemble.

To illustrate how C-2DES can be used to probe energy transfer in biological chromophores, we also generate phased 2D-spectra of Chl*a*, as shown in figure 4.9(b). Here, we show distinct Q_y vibrational signals. The peak at 665 nm is assigned to the 0-0 transition of Q_y band, based on the linear absorption spectrum and other reports in similar polar organic solutions [56-58]. The peaks at 610, 565, and 525 nm may arise from other vibrational Q_y transitions, i.e., 0-0, 0-1 and even 0-2 transitions. These four peaks are almost evenly spaced in energy domain and consistent with previous reports [57, 59]. The assignment of Q_x band has not been straightforward [60, 61]. Qx bands have been observed at ~570 nm [56, 59] as well as at ~620 nm [57, 60, 62]. Recent work to unify these assignments suggests that vibronic coupling can simultaneously explain all signals [61]. Similar to recent work on chlorophyll contained in the Photosystem I complex, we show little signal on the diagonal from the Q_x bands, but rather we see rapid growth of a crosspeak between Q_x and Q_y at very early times [42]. The 2D spectra also show significant excited state absorption in this system, likely arising from excitation to higher lying electronic states [63].

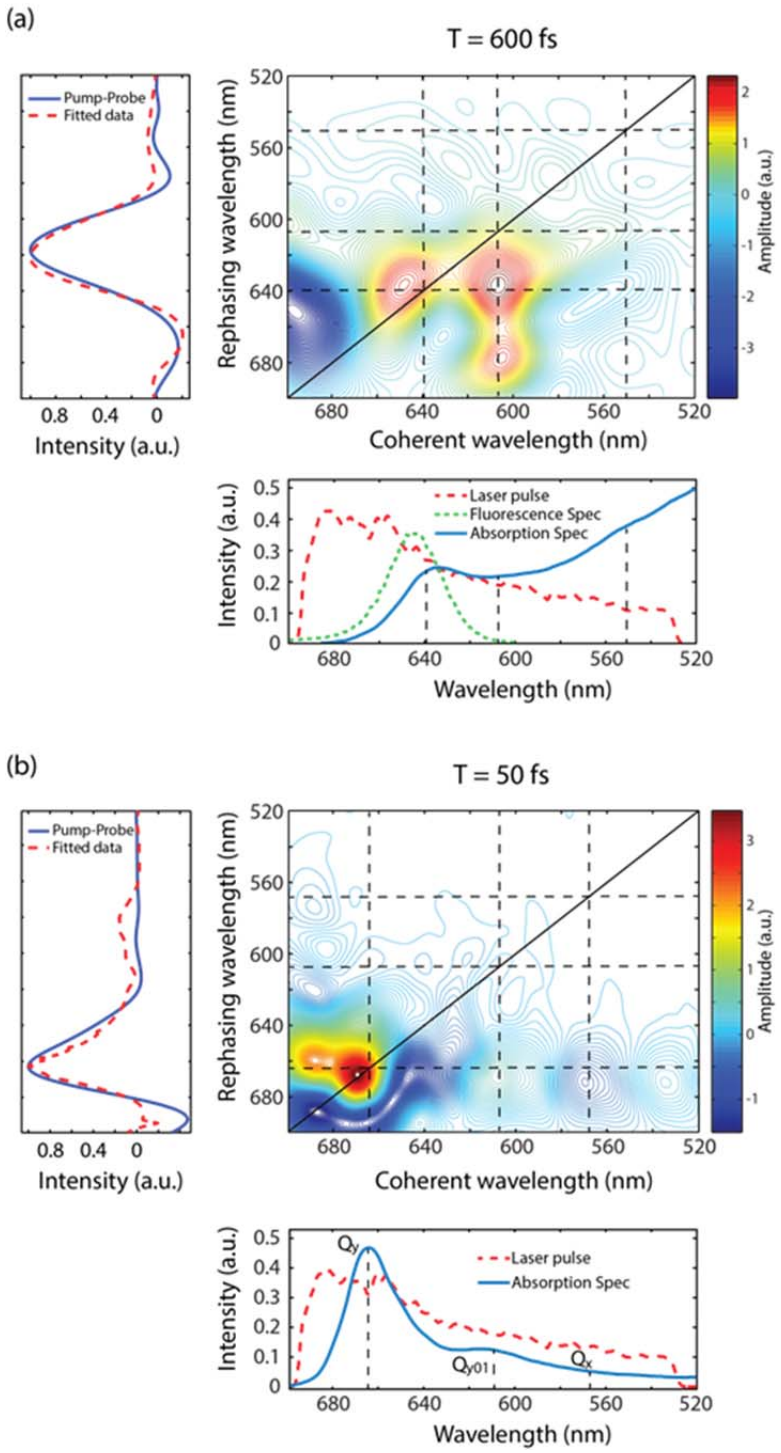

Figure 4.9 The phased two-dimensional spectrum of a) CdSe quantum dots at T=600 fs and b) Chl*a* at T=50 fs. We plot the pump-probe spectra and the projected 2D spectra on the left. Below each spectrum, we plot the laser pulse and the linear absorption spectrum of each system.

4.5 Conclusion

In this chapter, white light pulses are used to generate 2DES of CdSe QDs and Chl*a*. Using an all-reflective delay mechanism, we finely control the time delays without introducing phase nonlinearities. This method permits the use of broadband white light pulses for all interactions. By fitting the 2D spectra using pump-probe data taken with the same laser pulse, we extract phased 2D spectra for both CdSe QDs and Chl*a*, showing highly complex two-dimensional lineshapes, which will be explored more fully in future experiments.

4.6 Acknowledgments

The authors wish to thank Prof. Daniel Turner (NYU) for helpful guidance in our calculation of phase stability. The authors would like to thank NSF MRSEC (Grant No. DMR 08-02054), The Keck Foundation, AFOSR (Grant No. FA9550-09-1-0117), and DTRA (HDTRA1-10-1-0091) for supporting this work in part. JRC and PDD acknowledge support from the NSF GRFP. PDD was supported by the Graduate Program in Biophysical Sciences at the University of Chicago (NIH Grant T32 Eb009412).

REFERENCES

[1] J. Hybl, A. Albrecht, S. Faeder, D. Jonas, Two-dimensional electronic spectroscopy, Chem Phys Lett, 297 (1998) 307-313.

[2] D.M. Jonas, Two-Dimensional Femtosecond Spectroscopy, Annual Review of Physical Chemistry, 54 (2003) 425-463.

[3] M.L. Cowan, J.P. Ogilvie, R.J.D. Miller, Two-dimensional spectroscopy using diffractive optics based phased-locked photon echoes, Chem Phys Lett, 386 (2004) 184-189.

[4] T. Brixner, T. Mancal, I. Stiopkin, G. Fleming, Phase-stabilized two-dimensional electronic spectroscopy, J Chem Phys, 121 (2004) 4221-4236.

[5] M. Cho, Two-Dimensional Optical Spectroscopy, CRC press, Boca Raton, Fl, 2009.

[6] J.A. Davis, T.R. Calhoun, K.A. Nugent, H.M. Quiney, Ultrafast optical multidimensional spectroscopy without interferometry, J Chem Phys, 134 (2011).

[7] R.n. Augulis, D. Zigmantas, Detector and dispersive delay calibration issues in broadband 2D electronic spectroscopy, Journal of the Optical Society of America B: Optical Physics, 30 (2013) 1770-1774.

[8] U. Selig, F. Langhojer, F. Dimler, T. Lohrig, C. Schwarz, B. Gieseking, T. Brixner, Inherently phase-stable coherent two-dimensional spectroscopy using only conventional optics, Opt Lett, 33 (2008) 2851-2853.

[9] U. Selig, C.F. Schleussner, M. Foerster, F. Langhojer, P. Nuernberger, T. Brixner, Coherent two-dimensional ultraviolet spectroscopy in fully noncollinear geometry, Opt. Lett., 35 (2010) 4178-4180.

[10] Y. Zhang, K. Meyer, C. Ott, T. Pfeifer, Passively phase-stable, monolithic, all-reflective two-dimensional electronic spectroscopy based on a four-quadrant mirror, Opt Lett, 38 (2013) 356-358.

[11] T. Zhang, C. Borca, X. Li, S. Cundiff, Optical two-dimensional Fourier transform spectroscopy with active interferometric stabilization, Opt Express, 13 (2005) 7432-7441.

[12] L. Wang, G. Griffin, A. Zhang, F. Zhai, N. Williams, R. Jordan, G. Engel, Controlling quantum-beating signals in 2D electronic spectra by packing synthetic heterodimers on single-walled carbon nanotubes, Nature Chemistry, 9 (2017) 219-225.

[13] E. Harel, A. Fidler, G. Engel, Real-time mapping of electronic structure with single-shot two-dimensional electronic spectroscopy, Proceedings of the National Academy of Sciences of the United States of America, 107 (2010) 16444-16447.

[14] E. Harel, A. Fidler, G. Engel, Single-Shot Gradient-Assisted Photon Echo Electronic Spectroscopy, Journal of Physical Chemistry a, 115 (2011) 3787-3796.

[15] S. Yin, O. Leonov, F. Yu, V. Molotok, V. Kludzin, Design and fabrication of a 24-channel acousto-optic spatial light modulator, Applied Optics, 37 (1998) 7482-7489.

[16] S.-H. Shim, D.B. Strasfeld, Y.L. Ling, M.T. Zanni, Automated 2D IR spectroscopy using a mid-IR pulse shaper and application of this technology to the human islet amyloid polypeptide, Proceedings of the National Academy of Sciences, 104 (2007) 14197-14202.

[17] J. Myers, K. Lewis, P. Tekavec, J. Ogilvie, Two-color two-dimensional Fourier transform electronic spectroscopy with a pulse-shaper, Opt Express, 16 (2008) 17420-17428.

[18] P. Tyagi, J.I. Saari, B. Walsh, A. Kabir, V. Crozatier, N. Forget, P. Kambhampati, Two-Color Two-Dimensional Electronic Spectroscopy Using Dual Acousto-Optic Pulse Shapers for Complete Amplitude, Phase, and Polarization Control of Femtosecond Laser Pulses, The Journal of Physical Chemistry A, 117 (2013) 6264-6269.

[19] K. Iizuka, Elements of photonics, Wiley-Interscience, New York, N.Y., 2002.

[20] B.A. West, B.P. Molesky, P.G. Giokas, A.M. Moran, Uncovering molecular relaxation processes with nonlinear spectroscopies in the deep UV, Chem Phys, 423 (2013) 92-104.

[21] E. Harel, P.D. Long, G.S. Engel, Single-shot ultrabroadband two-dimensional electronic spectroscopy of the light-harvesting complex LH2, Opt Lett, 36 (2011) 1665-1667.

[22] D. Turner, Y. Hassan, G. Scholes, Exciton Superposition States in CdSe Nanocrystals Measured Using Broadband Two-Dimensional Electronic Spectroscopy, Nano Lett, 12 (2012) 880-886.

[23] E.E. Ostroumov, R.M. Mulvaney, R.J. Cogdell, G.D. Scholes, Broadband 2D Electronic Spectroscopy Reveals a Carotenoid Dark State in Purple Bacteria, Science, 340 (2013) 52-56.

[24] D. Kartashov, S. Alisauskas, A. Pugzlys, A. Voronin, A. Zheltikov, M. Petrarca, P. Bejot, J. Kasparian, J. Wolf, A. Baltuska, White light generation over three octaves by femtosecond filament at 3.9 mu m in argon, Optics Letters, 37 (2012) 3456-3458.

[25] D.E. Wilcox, F.D. Fuller, J.P. Ogilvie, Fast second-harmonic generation frequency-resolved optical gating using only a pulse shaper, Opt Lett, 38 (2013) 2980-2983.

[26] M. Nisoli, S. DeSilvestri, O. Svelto, Generation of high energy 10 fs pulses by a new pulse compression technique, Appl Phys Lett, 68 (1996) 2793-2795.

[27] M. Nisoli, G. Sansone, S. Stagira, C. Vozzi, S. De Silvestri, O. Svelto, Ultra-broadband continuum generation by hollow-fiber cascading, Appl Phys B-Lasers O, 75 (2002) 601-604.

[28] K. Yamane, Z. Zhang, K. Oka, R. Morita, M. Yamashita, A. Suguro, Optical pulse compression to 3.4 fs in the monocycle region by feedback phase compensation, Opt Lett, 28 (2003) 2258-2260.

[29] G. Steinmeyer, G. Stibenz, Generation of sub-4-fs pulses via compression of a white-light continuum using only chirped mirrors, Appl Phys B-Lasers O, 82 (2006) 175-181.

[30] H. Wang, Y. Wu, C. Li, H. Mashiko, S. Gilbertson, Z. Chang, Generation of 0.5 mJ, few-cycle laser pulses by an adaptive phase modulator, Opt Express, 16 (2008) 14448-14455.

[31] B. Xu, Y. Coello, V. Lozovoy, D. Harris, M. Dantus, Pulse shaping of octave spanning femtosecond laser pulses, Opt Express, 14 (2006) 10939-10944.

[32] B. Xu, J. Gunn, J. Dela Cruz, V. Lozovoy, M. Dantus, Quantitative investigation of the multiphoton intrapulse interference phase scan method for simultaneous phase measurement and compensation of femtosecond laser pulses, Journal of the Optical Society of America B-Optical Physics, 23 (2006) 750-759.

[33] D.B. Turner, K.W. Stone, K. Gundogdu, K.A. Nelson, Invited Article: The coherent optical laser beam recombination technique (COLBERT) spectrometer: Coherent multidimensional spectroscopy made easier, Rev Sci Instrum, 82 (2011).

[34] R. Trebino, K. DeLong, D. Fittinghoff, J. Sweetser, M. Krumbugel, B. Richman, D. Kane, Measuring ultrashort laser pulses in the time-frequency domain using frequency-resolved optical gating, Rev Sci Instrum, 68 (1997) 3277-3295.

[35] J. Sweetser, D. Fittinghoff, R. Trebino, Transient-grating frequency-resolved optical gating, Opt Lett, 22 (1997) 519-521.

[36] R. Trebino, Frequency-Resolved Optical Gating: The Measurement of Ultrashort Laser Pulses., Springer2002.

[37] M.K. Yetzbacher, N. Belabas, K.A. Kitney, D.M. Jonas, Propagation, beam geometry, and detection distortions of peak shapes in two-dimensional Fourier transform spectra, J Chem Phys, 126 (2007) 044511-044519.

[38] S. Mukamel, Principles of nonlinear optical spectroscopy, Oxford, New York, 1995.

[39] A. Zewail, Femtochemistry: Atomic-scale dynamics of the chemical bond, Journal of Physical Chemistry a, 104 (2000) 5660-5694.

[40] M. Drescher, M. Hentschel, R. Kienberger, M. Uiberacker, V. Yakovlev, A. Scrinzi, T. Westerwalbesloh, U. Kleineberg, U. Heinzmann, F. Krausz, Time-resolved atomic inner-shell spectroscopy, Nature, 419 (2002) 803-807.

[41] P. Kambhampati, Hot Exciton Relaxation Dynamics in Semiconductor Quantum Dots: Radiationless Transitions on the Nanoscale, Journal of Physical Chemistry C, 115 (2011) 22089-22109.

[42] J. Du, K. Nakata, Y. Jiang, E. Tokunaga, T. Kobayashi, Spectral modulation observed in Chl-a by ultrafast laser spectroscopy, Opt Express, 19 (2011) 22480-22485.

[43] J. Anna, E. Ostroumov, K. Maghlaoui, J. Barber, G. Scholes, Two-Dimensional Electronic Spectroscopy Reveals Ultrafast Downhill Energy Transfer in Photosystem I Trimers of the Cyanobacterium Thermosynechococcus elongatus, J Phys Chem Lett, 3 (2012) 3677-3684.

[44] V.I. Prokhorenko, A. Halpin, R.J.D. Miller, Coherently-controlled two-dimensional photon echo electronic spectroscopy, Opt Express, 17 (2009) 9764-9779.

[45] G. Panitchayangkoon, D. Hayes, K. Fransted, J. Caram, E. Harel, J. Wen, R. Blankenship, G. Engel, Long-lived quantum coherence in photosynthetic complexes at physiological temperature, Proceedings of the National Academy of Sciences of the United States of America, 107 (2010) 12766-12770.

[46] P.F. Tekavec, J.A. Myers, K.L.M. Lewis, F.D. Fuller, J.P. Ogilvie, Effects of chirp on two-dimensional Fourier transform electronic spectra, Opt Express, 18 (2010) 11015-11024.

[47] M. Li, J.P. Nibarger, C. Guo, G.N. Gibson, Dispersion-free Transient-grating Frequency-resolved Optical Gating, Applied Optics, 38 (1999) 5250-5253.

[48] G.D. Scholes, Selection rules for probing biexcitons and electron spin transitions in isotropic quantum dot ensembles, J. Chem. Phys., 121 (2004) 10104.

[49] S.L. Sewall, R.R. Cooney, K.E.H. Anderson, E.A. Dias, D.M. Sagar, P. Kambhampati, State-resolved studies of biexcitons and surface trapping dynamics in semiconductor quantum dots, J. Chem. Phys., 129 (2008) 084701.

[50] S.L. Sewall, A. Franceschetti, R.R. Cooney, A. Zunger, P. Kambhampati, Direct observation of the structure of band-edge biexcitons in colloidal semiconductor CdSe quantum dots, Phys. Rev. B: Condens. Matter, 80 (2009) 081310.

[51] K.W. Stone, K. Gundogdu, D.B. Turner, X. Li, S.T. Cundiff, K.A. Nelson, Two-Quantum 2D FT Electronic Spectroscopy of Biexcitons in GaAs Quantum Wells, Science, 324 (2009) 1169-1173.

[52] P. Kambhampati, Unraveling the Structure and Dynamics of Excitons in Semiconductor Quantum Dots, Accounts of Chemical Research, 44 (2010) 1-13.

[53] C. Wong, G. Scholes, Biexcitonic Fine Structure of CdSe Nanocrystals Probed by Polarization-Dependent Two-Dimensional Photon Echo Spectroscopy, Journal of Physical Chemistry a, 115 (2011) 3797-3806.

[54] D.B. Turner, Y. Hassan, G.D. Scholes, Exciton Superposition States in CdSe Nanocrystals Measured Using Broadband Two-Dimensional Electronic Spectroscopy, Nano Lett, 12 (2011) 880-886.

[55] C.Y. Wong, G.D. Scholes, Using two-dimensional photon echo spectroscopy to probe the fine structure of the ground state biexciton of CdSe nanocrystals, Journal of Luminescence, 131 (2011) 366-374.

[56] P. Kambhampati, Multiexcitons in Semiconductor Nanocrystals: A Platform for Optoelectronics at High Carrier Concentration, Journal of Physical Chemistry Letters, 3 (2012) 1182-1190.

[57] R.E. Blankenship, Molecular Mechanisms of Photosynthesis, Blackwell Science: Oxford, Malden, MA, 2002.

[58] M. Ratsep, J. Linnanto, A. Freiberg, Mirror symmetry and vibrational structure in optical spectra of chlorophyll a, J. Chem. Phys., 130 (2009) 194501-194511.

[59] J. Du, T. Teramoto, K. Nakata, E. Tokunaga, T. Kobayashi, Real-Time Vibrational Dynamics in Chlorophyll a Studied with a Few-Cycle Pulse Laser, Biophys J, 101 (2011) 995-1003.

[60] J.L. Hughes, B. Conlon, T. Wydrzynski, E. Krausz, The assignment of Qy(1,0) vibrational structure and Qx for chlorophyll a, Physics Procedia, 3 (2010) 9.

[61] I. Renge, K. Mauring, P. Sarv, R. Avarmaa, Vibrationally Resolved Optical-Spectra of Chlorophyll Derivatives in Different Solid Media, Journal of Physical Chemistry, 90 (1986) 6611-6616.

[62] J.R. Reimers, Z.L. Cai, R. Kobayashi, M. Ratsep, A. Freiberg, E. Krausz, Assignment of the Q-Bands of the Chlorophylls: Coherence Loss via Q(x) - Q(y) Mixing, Sci Rep-Uk, 3 (2013).

[63] M. Umetsu, Z.Y. Wang, M. Kobayashi, T. Nozawa, Interaction of photosynthetic pigments with various organic solvents - Magnetic circular dichroism approach and application to chlorosomes, Biochimica Et Biophysica Acta-Bioenergetics, 1410 (1999) 19-31.

[64] L. De Boni, D.S. Correa, F.J. Pavinatto, D.S. dos Santos, C.R. Mendonca, Excited state absorption spectrum of chlorophyll a obtained with white-light continuum, J Chem Phys, 126 (2007).

5 Probing Early Time Electronic Relaxation Dynamics in CdSe, CdSe/ZnS, CdSe/ZnS/CdSe Quantum Dots

In the chapter 2, a series of CdSe core, CdSe/ZnS core-shell, and CdSe/ZnS/CdSe core-shell-shell quantum dots were synthesized. We are now probing the early time electronic dynamics of all these samples, using a combination of an all-reflective ultrafast broadband two-dimensional electronic spectroscopy and a pump-probe spectroscopy. Clean features related to the first two lowest-energy excitons were obtained on phased 2D spectra, and used to explore the influence of surface environment on the electronic relaxation in very early time.

5.1 Background introduction

Quantum dots (QDs) are crystals of a semiconductor material, made up of hundreds to many thousands of atoms [1-3] and passivated with an organic outer layer of surfactant molecules (ligands) [4, 5]. In QDs whose size is reduced to a few nanometers, which is the same magnitude as the de Broglie wavelength of the electron wave function, the band gap is increased compared with that of the bulk and the electron energy levels are quantized and discrete. This effect is known as the quantum confinement effect [6] and was elaborately discussed in the chapter 1. In quantum physics, this effect can be modeled as a small sphere confined in three dimensions. Thus, for a specific QDs chemical composition, the electronic and optical properties are affected by size and shape, which determine the potential energy of the well.

The electronic structure of CdSe QDs near the band edge has been described previously [7-9]. Generally, when light is absorbed by a semiconductor sample, the electron will be excited from

the valence band to the conduction band, creating an electron-hole pair (exciton). These discrete states in the valance and conduction bands are assigned a principal quantum number, an angular momentum state, and a total angular momentum term [8]: $1S_{3/2}$, $1P_{3/2}$, and $2S_{3/2}$ to the three highest hole states, and 1S, 1P to the two lowest electronic states. The two lowest-energy excitons labeled as $|X_1\rangle$ and $|X_2\rangle$, correspond to $1S_{3/2}(h) \rightarrow 1S(e)$ and $2S_{3/2}(h) \rightarrow 1S(e)$ electron-hole pairs. In this study, we probe these two excitonic states in different composites of wurtzite CdSe core-based QDs.

When the size of the QDs is reduced to a few nanometers, the surface-to-volume ratio is extremely high. The highly populated sphere of surface atoms is coordinated via interactions with stabilizing ligands. However, these organically passivated QDs exhibit a significant degree of surface trap states (energetically localized within the energy gap), which challenges their applicability in future technologies [10]. Surface trap states act as channels for fast non-radiative de-excitation of high energy photo-excitatons (hot excitons) [11-13], reducing both the mobility and the diffusion length of charge carriers across QDs [13]. Thereby, these surface defects result in quenching of the QD photoluminescence and reduction of the fluorescence quantum yield (QY).

Recent work has shown that that the low-lying (near band edge) hole relaxation is dominated by the ligand-involved non-radiative pathway [14-16]. In order to tune the hot exciton relaxation in the current study, we apply a layer of ZnS, another semiconductor material with a much larger bandgap (3.61 eV compared with 1.74 eV of CdSe in bulk), as a shell over the CdSe QDs to protect them from the surface environment. Since the first three excitons of CdSe (those observable within our spectrum range) lay in the bandgap of ZnS, the shell is merely used to passivate the surface of the CdSe core and isolate it from the organic ligands. Moreover, we then

apply another CdSe layer to cover the CdSe/ZnS core shell QDs to interact with these coordinated ligands, to see if the excitonic relaxation in the core can be mediated via the coupling between the two CdSe heterostructures.

CdSe quantum dots have been extensively studied using various linear spectroscopic methods such as linear absorption and photoluminescence [17-19]. Since the linear absorption or emission signal comes from a weak light-matter interaction with one incident radiation field, these spectra are plotted on a single frequency axis. In a complex system with many interactions or in highly inhomogeneous ensembles, these linear spectra will be congested and poorly resolved. In addition, linear spectroscopies are very limited in terms of probing fast dynamics, especially the fast relaxations that exist in CdSe QDs.

Nonlinear spectroscopy provides a way to resolve this dilemma by using multiple light-matter interactions and controlling frequency or time-delay, to correlate different spectral features [20-22]. Specifically, four-wave mixing methods, such as transient absorption [23-25] (TA), photon echo peak shift [26, 27] and two-dimensional electronic spectroscopy (2DES) [3, 28-30] have been performed to measure both electronic structure and dynamics in QDs. In this the current, we apply broadband 2DES to probe ultrafast relaxation dynamics and nonlinear response of the two lowest-lying excited states in CdSe, CdSe/ZnS core-shell, and CdSe/ZnS/CdSe core-shell-shell QDs. We investigate the early time electronic relaxation of these samples using ultra short pulses (8 fs), and illustrate how surrounding ligands mediate the fast electronic behaviors.

5.2 Experimental Section

The 2DES setup was adapted from our previous reports [8, 31, 32], and described in the chapter 4. We focused the 2.9 W, 5.0 kHz, 35 fs FWHM output laser of a Ti:sapphire regenerative amplifier (Legend Elite, Coherent) into 2 atm argon gas to generate broadband white light. A hot mirror was used to filter the white light, producing a spectrum with FWHM from 480 to 700 nm (figure 5.1). We then temporally compressed it using the Multiphoton Intrapulse Interference Phase Scan (MIIPS) method [33] with a spatial light modulator (SLM, from Biophotonic Solutions Inc). The beam split into four pulses and the timings were controlled by an all-reflective 2DES system [31]. All four well collimated pulses (incident power of 1.5 nJ/pulse for the first three pulses) were focused onto a 100 μm diameter spot at the sample position using a silver parabolic mirror. We measured the pulse durations of ~8-10 fs at the sample position, using transient-grating frequency resolved optical gating (TG-FROG) (figure 5.2). Three laser pulses interact with the sample, generating a third-order signal in the phase-matched direction ($\boldsymbol{k_s}=-\boldsymbol{k_1}+\boldsymbol{k_2}+\boldsymbol{k_3}$): The time delay between the first two pulses is coherence time, $\boldsymbol{\tau}$, and the time separation between pulse 2 and 3 is known as waiting time, $\boldsymbol{T}$, which is similar to the time delay in TA spectroscopy. After a rephasing time $\boldsymbol{t}$ (the time delay between pulse 3 and the signal), the signal is emitted in a phase-matched direction and heterodyne detected with the fourth pulse (local oscillator, LO) which is attenuated five orders of magnitude and recorded using a commercial Shamrock spectrometer and Newton camera (Andor Technology, Inc).

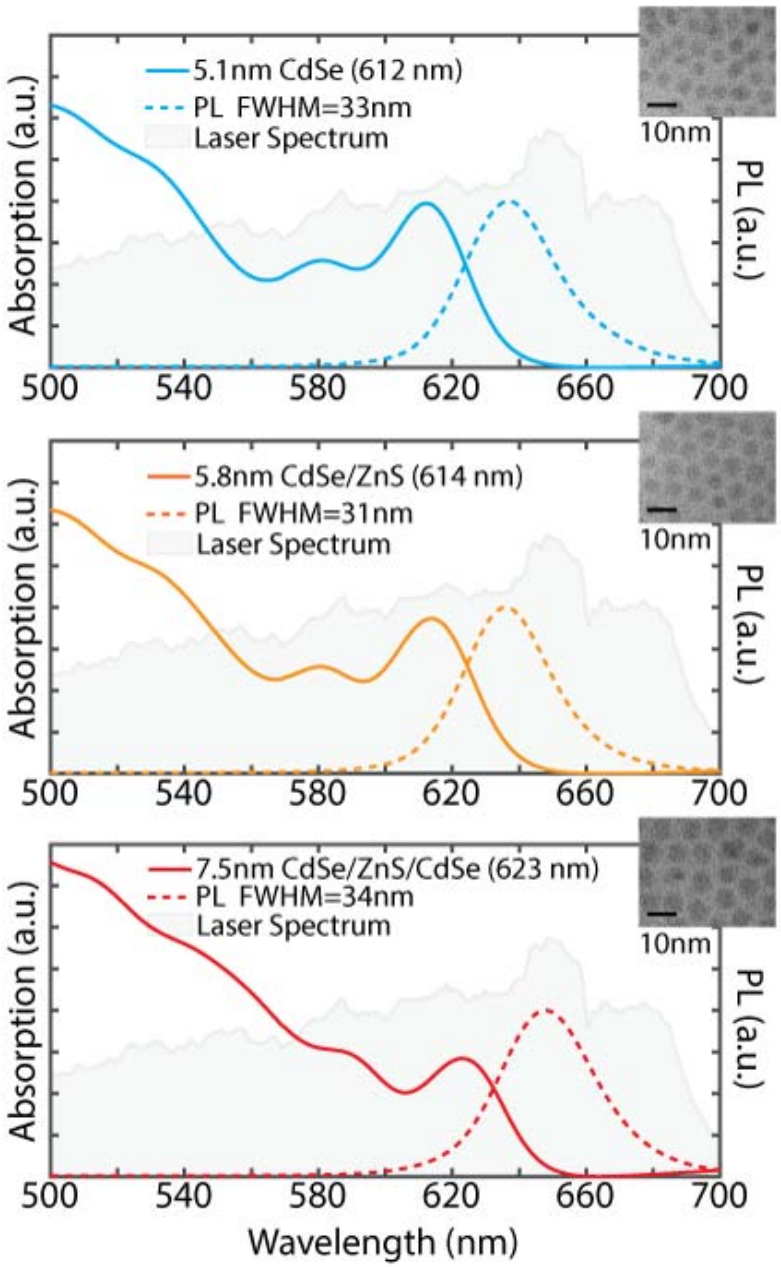

Figure 5.1 UV-Vis absorption spectra (solid line) and photoluminescence (PL) (dashed line, excited at 400 nm) of CdSe core-only (top), CdSe/ZnS (middle), and CdSe/ZnS/CdSe (bottom) quantum dots are plotted. The grey shadow shows the ultrafast broadband spectrum applied to interrogate the system (taken at the sample position using spectrometer from Ocean optics). The TEM image of each nanocrystal is displayed on the upper-right corner.

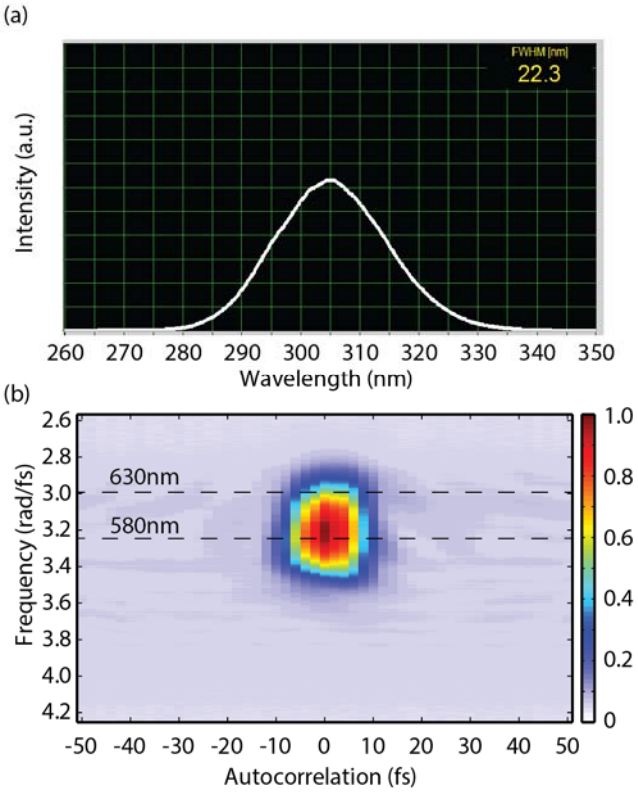

Figure 5.2 (a) Second harmonic generation from beta barium borate (BBO); (b) Transient-grating frequency resolved optical gating (TG-FROG) in toluene solvent.

In the 2DES measurement, waiting times $\boldsymbol{T}$ were scanned from -20 to 200 fs with a step of 5 fs, to capture the early time dynamics. We scanned the coherence time $\boldsymbol{\tau}$ from -90 to 90 fs with a step of 1.5 fs. At each $\boldsymbol{\tau}$, we collect an interferogram on the camera in $\boldsymbol{\omega_t}$, as well as several reference signals for scatter subtraction [34]. We first Fourier transformed over camera frequency $\boldsymbol{\omega_t}$ to create a time-time plot and then applied a window function in the rephasing time $\boldsymbol{t}$ domain to eliminate scatter and homodyne components. Finally, Fourier transforms over both $\boldsymbol{\tau}$ and $\boldsymbol{t}$ domains yielded 2D electronic spectra in the frequency-frequency domain. All 2DES measurements were run at room temperature. At least three sets of parallel data were collected

for each sample. All QDs solutions were contained in a 200 μm path length sample cell (Starna Cell, fused quartz), with a concentration about 0.3 OD.

The output pulse from MIIPS was guided into the pump-probe setup and compressed separately for the pump-probe measurement. The 5.0 kHz pump beam was chopped at 2.5 kHz, so that the pump-probe and probe-only spectra were collected alternatively on a high-speed line scan camera (Horiba). The pump-probe data was acquired for all time delays matching the waiting times of the 2DES measurement. Each individual 2D spectrum at different waiting time is phased to corresponding pump-probe data via applying the projection-slice theorem illustrated elsewhere [8, 34]. Through fitting the projection of the real part of each 2D spectrum onto the ω_t axis to the TA spectrum, we acquired the real 2D spectrum that enables the assignment of the sign of peaks in 2D spectra to excited state absorption (ESA, negative feature), ground state bleach (GSB positive), or stimulated emission (SE, positive) pathways.

5.3 Spectral features and early time dynamics

Starting with the CdSe nanocrystal core (5.1 nm), CdSe/ZnS core-shell (5.8 nm) and CdSe/ZnS/CdSe core-shell-shell (7.5 nm) structures were synthesized by applying a ZnS shell to the CdSe nanocrystal core, and then applying another two CdSe layers around the ZnS shell. In figure 5.1, we show the linear spectra of the series of CdSe core, CdSe/ZnS core-shell, and CdSe/ZnS/CdSe core-shell-shell structures. We focus on these three QD structures in this paper to explore the shell influence on the early time electronic dynamics. We first fit these absorption spectra using multi-Gaussian components as shown in the chapter 2, figure 2.2, convincingly assigning the peak locations of these exciton energies. The first excitation peak ($1S_{3/2}$(h)→1S(e),

$|X_1>$) red shifts, from 613 nm to 614 nm, after the application of the ZnS shell, in agreement with previous reports [35, 36]. The addition of the ZnS layer to the CdSe core makes the wave function more delocalized and the band gap closer, resulting in this red shift (figure 5.1, middle panel). After the application of the CdSe shell, the electron orbital of the CdSe core is even less bounded and it can partially leak into the outside CdSe layer due to the coupling between the core and the outside CdSe shell. Therefore, the first excitation peak further shifts to 624 nm (figure 5.1, bottom panel). Both the absorption spectra and photoluminescence exhibit the same trend for the second/third excitons and the band gap. The two lowest-energy excitons are well resolved in the absorption spectrum for all three QDs, indicating a very narrow size distribution. The state- and size- dependent inhomogeneous lineshape was deduced in the study by Caram et al [8]. TEM images reveal that the diameter measurements of these monodispersed QDs are 5.1 nm, 5.8 nm, and 7.5 nm, respectively (figure 5.1), corresponding to the consecutive application of one layer of ZnS and two layers of CdSe shell. In their 2005 publication, Battaglia et al [37] describe how one layer of ZnS shell is not thick enough to completely isolate the CdSe shell from the core, leading to the significant red shift that were observed in the current experiment (figure 5.1). Here, we used a broadband laser spectrum (480 - 700 nm; grey shadow in figure 5.1), which is capable of covering the first three excitons for all three QDs.

Ultrafast TA, or pump-probe, spectroscopy is a commonly used non-linear spectroscopy method that measures changes in the absorbance/transmittance in the sample of interest. The pump-probe spectrum can be interpreted as a four-wave mixing method in the language of time-dependent perturbation theory. The method is related to 2DES: the pump pulse (similar to the first two pulses in 2DES, $\boldsymbol{\tau} = 0$) interacts with the sample twice to initiate dynamics for a specific state; after a delay of $\boldsymbol{T}$ (waiting time), the probe pulse interrogates the sample and the third order

response signal emits in the same direction as the probe pulse; this signal is then heterodyned with the probe pulse and detected by a spectrometer, generating a one-dimensional frequency resolved spectrum for each waiting time ***T***. The pump-probe spectrum reflects different pathways such as the GSB, SE, and ESA processes. Thus, both pump-probe spectroscopy and 2DES explore the same nonlinear processes.

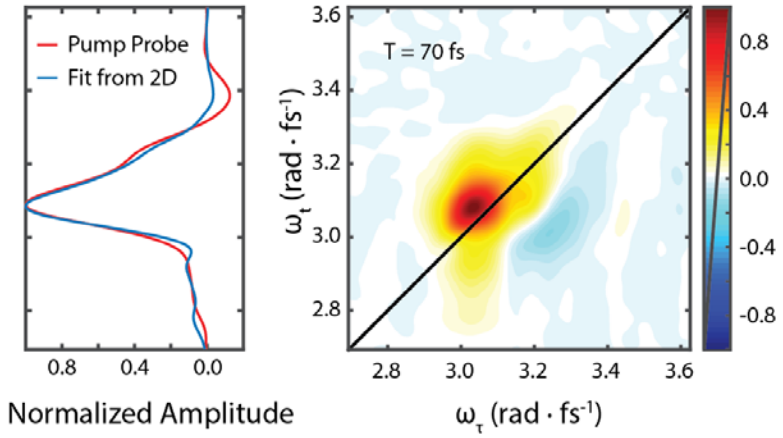

Figure 5.3 The fitting result when phasing 2D spectrum using pump-probe data. Three features were observed for pump-probe spectrum: 613nm (3.07 rad·fs-1) peak, 582nm (3.24 rad·fs-1) shoulder, and 558nm (3.38 rad·fs-1) negative peak. The blue line shows the summed 2D spectrum towards left.

In our experiment, the transmittance of the sample was recorded as a function of time delay ***T*** between the pulse for excitation (pump) and the pulse for measuring the transmittance (probe). We illustrate the high degree of overlap between the 2DES and pump-probe spectra in figure 5.3. The features of the pump-probe spectrum of the CdSe QDs are similar to those in previous reports [8, 9, 24, 29, 38, 39]. The two well resolved positive features at 613 nm and 582 nm exactly match the first two excitations read from the absorption spectrum in figure 5.1. The features represent the emission of the first and second excitons, respectively, coming from the GSB and SE pathways. These two features in the TA spectrum (figure 5.3, left panel) were

discussed in detail in the report by Zhang et al [9]. In addition, the negative feature at 558 nm reflects an ESA pathway. In the case of CdSe QDs, the ESA corresponds to the transition from a single excitonic state ($|X_1\rangle$ or $|X_2\rangle$) to a bi-excitonic ($|X_1, X_3\rangle$ or $|X_2, X_3\rangle$) state. Due to the coupling between these two single excitons, the bi-excitonic energy is lower than the total energy of two individual excitons; this leads to a red shift (from 534 nm to 558 nm, 0.1 eV) representing the bi-exciton binding energy. This shift is in agreement with a previous report [40].

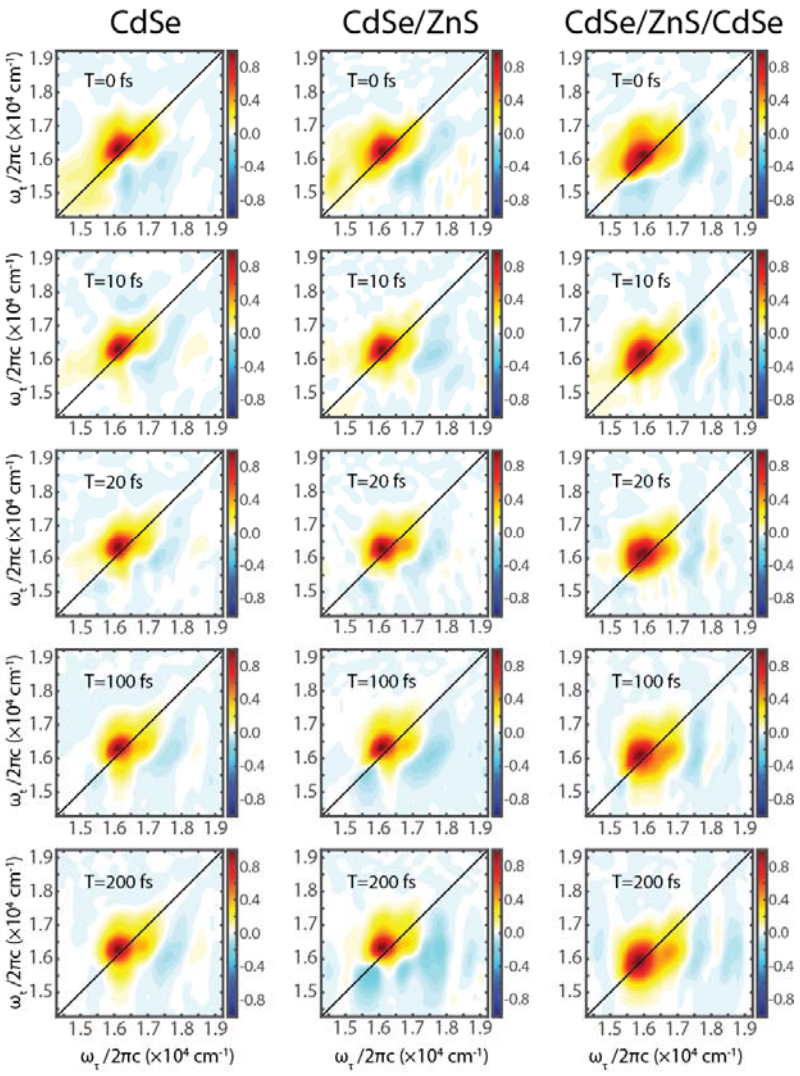

Figure 5.4 Phased 2DES of CdSe (left), CdSe/ZnS (middle), CdSe/ZnS/CdSe (right) quantum dots sampled over a range of waiting times. The color scale in each spectrum is individually normalized to maximum intensity at that waiting time.

We then phased the individual 2DES spectra to their corresponding pump-probe spectra using the projection-slice theorem. Phasing enables assignment of the sign of each peak in 2DES to GSB, SE or ESA pathways. In figure 5.4, we show a sequence of phased two-dimensional spectra taken at $\boldsymbol{T}$ = 0, 10, 20, 100 and 200 fs (top to bottom), for CdSe, CdSe/ZnS and CdSe/ZnS/CdSe QDs (left to right). Each 2DES spectrum can be interpreted using a simple "energy-in/energy-out" picture: the coherent frequency axis ($\boldsymbol{\omega_\tau}$) represents the energy that goes into the system upon excitation, and the rephasing frequency axis ($\boldsymbol{\omega_t}$) represents the energy of the signal that comes out of the system after a specific waiting time $\boldsymbol{T}$. In these two-dimensional electronic spectra, two significant features appear along the diagonal, corresponding to the two lowest-energy excitations in the linear absorption spectra. In CdSe core-only QDs (figure 5.4; left column), an intense positive peak centered near 16,300 cm^{-1} (613 nm) on the rephasing axis indicates the GSB/SE pathways associated with the first exciton. The peak position is slightly left of the diagonal, with a deviation of approximately 200 cm^{-1}, close to the frequency of phonon mode (210 cm^{-1}). This phonon mode was detected clearly both in the long waiting time beating frequency plot and Raman spectra (figure 2.4). This peak position offset and the phonon mode frequency are the same as those observed in previous studies [3, 28, 41]. Since these off-diagonal phenomena do not exist in the blank experiment or reference sample (PM 650), we assume that they are not due to miscalibration, but to the phonon-exciton coupling states. This diagonal peak becomes more round in shape at $\boldsymbol{T}$ = 200 fs due to homogenous broadening processes. The signal related to the second exciton elongates along the diagonal, centered near 17,100 cm^{-1}. A similar pattern for these two diagonal features is observed for CdSe/ZnS (16,300 cm^{-1} and 17,100 cm^{-1}; figure 5.4, middle column) and CdSe/ZnS/CdSe (16,000 cm^{-1} and 16,800 cm^{-1}; figure 5.4, right column) QDs. The peak positions of these two features also follow the red-

shift trend that is seen in the linear absorption spectrum. A substantially positive cross peak below the diagonal, matching the energy of these two excitons, is consistent across all three sample types. In addition, we observe a number of negative features above and below the diagonal that are the results of bi-exciton processes. These features were discussed by Turner et al [3].

In this work, we focus on the first two lowest-energy excitons in our series of CdSe-based QDs because: (1) both excited states are well resolved in the absorption spectrum, making it possible to correctly assign them in the 2DES spectrum; (2) the laser spectrum used in the 2DES is well compressed from 560 to 680 nm (the second harmonic generation from beta barium borate and TG-FROG are shown in the figure 5.2), making it ideal to probe the first two excitons; and (3) the features shown in 2DES associated with the first two excitons are clear and in line with our expectations.

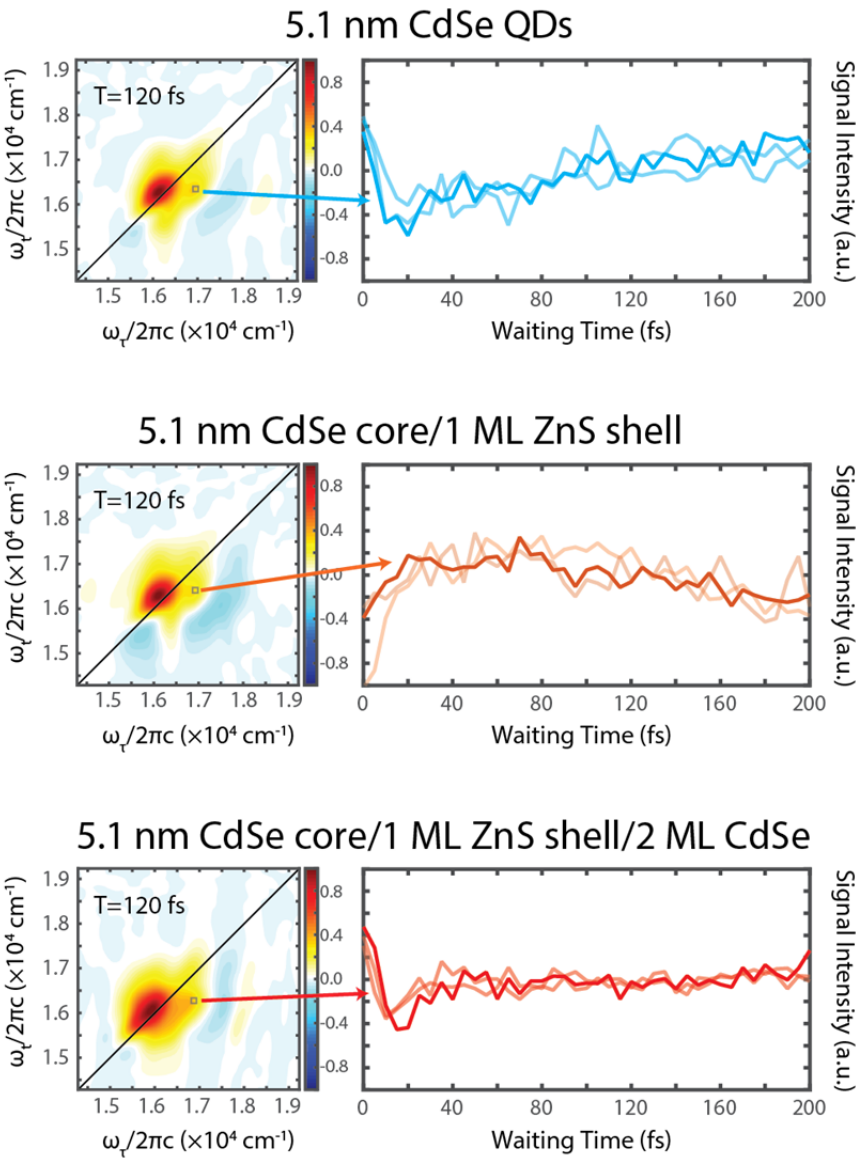

Figure 5.5 Intensity of the exciton 1-2 cross peak below the diagonal in phased 2DES of CdSe (top), CdSe/ZnS (middle), and CdSe/ZnS/CdSe (bottom) QDs plotted against waiting time, from 0 to 200 fs. The intensity signals over a square centered at the cross peak position with a size of 100 cm-1 were summed to minimize the signal fluctuation. For each diagram, left shows the 2DES at T = 120 fs, and right shows the trace of the cross peak intensity over waiting time. Light colors indicate other two parallel experimental results.

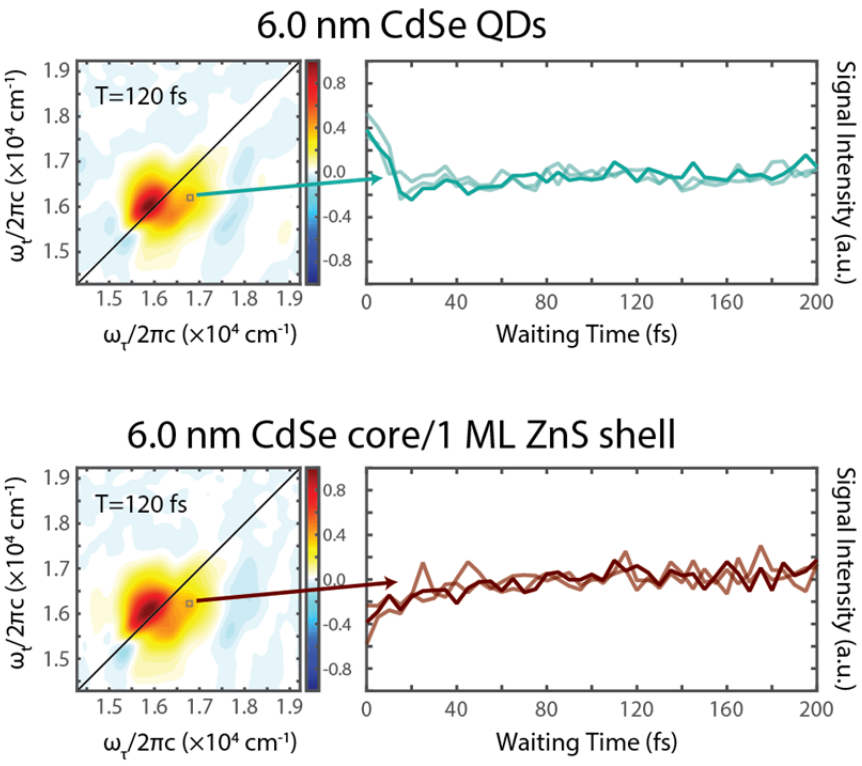

Figure 5.6 Intensity of the exciton 1-2 cross peak below the diagonal in phased 2DES of the larger CdSe (top), and larger CdSe/ZnS (bottom) QDs plotted against waiting time, from 0 to 200 fs.

Relaxation dynamics are measured by assigning changes in the observed intensity of spectroscopic features over time. The most interesting result of this study is the time dependence of the cross peak below the diagonal as a function of waiting time ***T***. This cross peak is assigned to the coupling between the two lowest-energy excitons. The evolution of the amplitude over time of the 2DES spectra at this cross peak position is shown in figure 5.5. The top panels in figure 5.5 display the trace of the cross peak extracted from 2DES of the CdSe-core only QDs (diameter = 5.1 nm). We combined the signal intensities from a small area (grey square shown at the peak position) to represent the intensity on the trace. The cross peak signal is most intense at zero waiting time, decreasing sharply to a local minimum at ***T*** = 20 fs, after which it rises again slowly. Two parallel experimental results are shown in a light color. This cross peak feature at

zero waiting time has been reported in previous studies [3, 28]. A study by Griffin et al. attributed this feature to artifacts derived from Fourier windowing, scatter subtraction, or contributions from solvent [28]. However, this cross peak feature does not exist in the separate, solvent-only experiment or in the reference sample (PM650, laser dye). Our results are in agreement with the results from Turner et al [3], for the early time traces of this cross peak from both the small CdSe (5.1 nm; figure 5.5, top panel) and the larger one (6.0 nm; figure 5.6 top panel). We could even catch a similar beating pattern of coherence for the first 50 fs for the larger CdSe QDs (the size is more close to that used by Turner), with a close coherent frequency (half period of 20 fs, 103 meV), matching the coherent energy (582nm-613nm, 108 meV).

When the ZnS shell is applied around the CdSe core, we no longer see this strong cross peak at zero waiting time (figure 5.5, middle panel). Instead, the signal increases to its maximum during the first 70 fs, and then decreases slowly. After applying another two layers of CdSe as the second shell, we see early time dynamics at the cross peak similar to those seen with the CdSe core-only QDs: the signal intensity maximizes at zero, decays quickly during the first 20 fs, and then increases (figure 5.5, bottom panel).

Following the "energy-in/energy-out" interpretation of 2DES described above, we expect to observe energy transfer from the $|X_2\rangle$ state into the $|X_1\rangle$ state as an exponential increase in signal at the cross coordinates. Indeed, we do observe this trend for both CdSe/ZnS core-shell samples (5.8 nm and 6.6 nm) across all experiments.

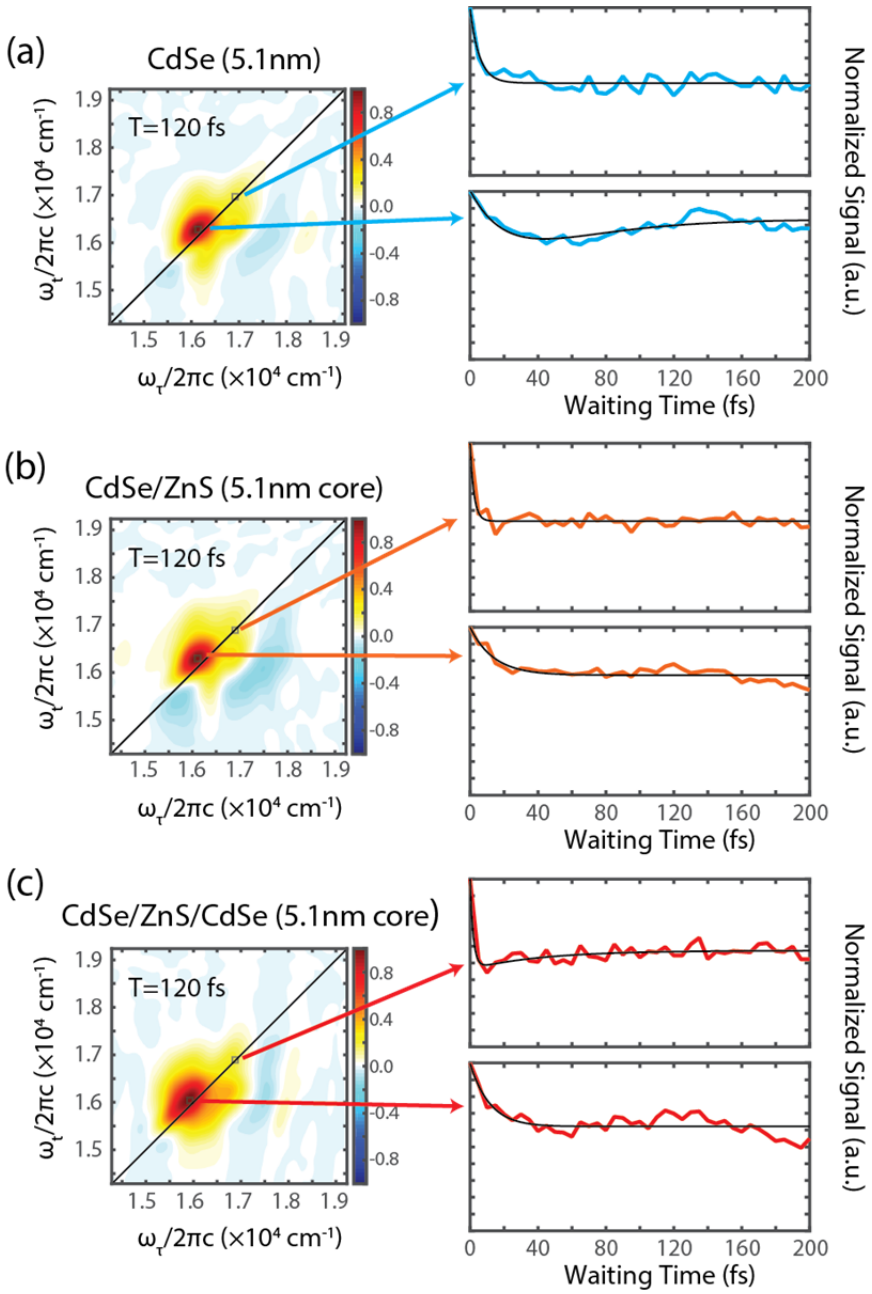

Figure 5.7 The relaxation of diagonal peaks during early waiting times from 0 to 200 fs, for (a)CdSe (5.1 nm) (b)CdSe/ZnS (5.1 nm core) and (c)CdSe/ZnS/CdSe (5.1 nm core)

To explain the different relaxation dynamics between the different QD samples at very early times, we propose that there are two pathways for the relaxation from $|X_2\rangle$ to $|X_1\rangle$. The Auger-like mechanism, mentioned above, exists in all three samples, while a ligand-assisted surface

process only occurs in ligand-surrounded CdSe core or in the CdSe/ZnS/CdSe core-shell-shell nanocrystals. One layer alone of ZnS is not enough to isolate the core from the outside shell, but we can consider that the CdSe/ZnS/CdSe sample acts like another CdSe core-only QDs. The Auger-like and surface process mechanisms compete in CdSe core-only QDs, while the Auger-like mechanism is the dominant mechanism in CdSe/ZnS core-shell structures. According to previous reports, the surface process takes about 15 fs [3], while the Auger-like process lasts more than 100 fs [8]. We propose that for CdSe cores, after excitation to the second exciton $|X_2>$, the exciton will relax to the lower exciton $|X_1>$ almost instantly. In the figure 5.7, we plot the trace of the diagonal peak of the exciton $|X_2>$ and it relaxes dramatically within 5-10 fs. Then the exciton $|X_1>$ further decays to band edge or trap states, assisted by interaction with the ligands. However, this mechanism happens only at the surface of the QD. At the same time, the Auger-like mechanism facilitates the relaxation, and spectrally we can see the increase in intensity after 20 fs. This early time feature, in which the signal intensity decreases and increases, was observed in both the 5.1 nm and 6.0 nm CdSe core-only QDs, and in the CdSe/ZnS/CdSe core-shell-shell sample (figure 5.5, top panel; figure 5.6, top panel; and figure 5.5, bottom panel, respectively). However, we can only detect a single exponential decay for this relaxation in both CdSe/ZnS core-shell samples (5.8 nm and 6.6 nm), which suggests that the surface process is not permitted after introduced the ZnS shell on the surface.

5.4 Conclusion

In this work, we synthesized five quantum dots: a series of CdSe, CdSe/ZnS, and CdSe/ZnS/CdSe based on a small CdSe core (5.1 nm in diameter); and another CdSe and

CdSe/ZnS using a larger core (6.0 nm). Both TEM and linear absorption spectrum suggest a narrow size distribution for all samples. We then performed pump-probe and two-dimensional electronic spectroscopy using broadband ultrafast laser pulses. All two-dimensional spectra were phased, revealing clearly resolved features for the two lowest-energy excitons. For CdSe core-only QDs, the static characteristics or dynamics of these features in our results are in agreement with results in previous reports. After the application of the ZnS shell, the relaxation dynamics for these two excitons varies because the shell layer will isolate the core from ligands, which can act as efficient moderators for the exciton relaxation. The application of the second CdSe shell yields a relaxation trace similar to that of the simple CdSe core, due to the coupling between the core and the outside shell. The results show that in the core-shell or even core-shell-shell QDs, the relaxation processes are affected by the surface defects or ligands.

REFERENCES

[1] A. Alivisatos, Semiconductor clusters, nanocrystals, and quantum dots, Science, 271 (1996) 933-937.

[2] P. Reiss, M. Protiere, L. Li, Core/Shell Semiconductor Nanocrystals, Small, 5 (2009) 154-168.

[3] D. Turner, Y. Hassan, G. Scholes, Exciton Superposition States in CdSe Nanocrystals Measured Using Broadband Two-Dimensional Electronic Spectroscopy, Nano Letters, 12 (2012) 880-886.

[4] T. Inerbaev, A. Masunov, S. Khondaker, A. Dobrinescu, A. Plamada, Y. Kawazoe, Quantum chemistry of quantum dots: Effects of ligands and oxidation, Journal of Chemical Physics, 131 (2009).

[5] M. Peterson, L. Cass, R. Harris, K. Edme, K. Sung, E. Weiss, M. Johnson, T. Martinez, The Role of Ligands in Determining the Exciton Relaxation Dynamics in Semiconductor Quantum Dots, Annual Review of Physical Chemistry, Vol 65, 65 (2014) 317-339.

[6] W. Buhro, V. Colvin, Semiconductor nanocrystals - Shape matters, Nature Materials, 2 (2003) 138-139.

[7] A. Alivisatos, A. Harris, N. Levinos, M. Steigerwald, L. Brus, ELECTRONIC STATES OF SEMICONDUCTOR CLUSTERS - HOMOGENEOUS AND INHOMOGENEOUS BROADENING OF THE OPTICAL-SPECTRUM, Journal of Chemical Physics, 89 (1988) 4001-4011.

[8] J. Caram, H. Zheng, P. Dahlberg, B. Rolczynski, G. Griffin, D. Dolzhnikov, D. Talapin, G. Engel, Exploring size and state dynamics in CdSe quantum dots using two-dimensional electronic spectroscopy, Journal of Chemical Physics, 140 (2014).

[9] C. Zhang, T. Do, X. Ong, Y. Chan, H. Tan, Understanding the features in the ultrafast transient absorption spectra of CdSe quantum dots, Chemical Physics, 481 (2016) 157-164.

[10] A. Almeida, A. Sahu, A. Riedinger, D. Norris, M. Brandt, M. Stutzmann, R. Pereira, Charge Trapping Defects in CdSe Nanocrystal Quantum Dots, Journal of Physical Chemistry C, 120 (2016) 13763-13770.

[11] D. Barkhouse, A. Pattantyus-Abraham, L. Levina, E. Sargent, Thiols Passivate Recombination Centers in Colloidal Quantum Dots Leading to Enhanced Photovoltaic Device Efficiency, Acs Nano, 2 (2008) 2356-2362.

[12] A. Ip, S. Thon, S. Hoogland, O. Voznyy, D. Zhitomirsky, R. Debnath, L. Levina, L. Rollny, G. Carey, A. Fischer, K. Kemp, I. Kramer, Z. Ning, A. Labelle, K. Chou, A. Amassian, E. Sargent, Hybrid passivated colloidal quantum dot solids, Nature Nanotechnology, 7 (2012) 577-582.

[13] D. Zhitomirsky, O. Voznyy, S. Hoogland, E. Sargent, Measuring Charge Carrier Diffusion in Coupled Colloidal Quantum Dot Solids, Acs Nano, 7 (2013) 5282-5290.

[14] P. Guyot-Sionnest, B. Wehrenberg, D. Yu, Intraband relaxation in CdSe nanocrystals and the strong influence of the surface ligands, Journal of Chemical Physics, 123 (2005).

[15] R. Cooney, S. Sewall, K. Anderson, E. Dias, P. Kambhampati, Breaking the phonon bottleneck for holes in semiconductor quantum dots, Physical Review Letters, 98 (2007).

[16] P. Kambhampati, Unraveling the the Structure and Dynamics of Excitons in Semiconductor Quantum Dots, Accounts of Chemical Research, 44 (2011) 1-13.

[17] C. Murray, D. Norris, M. Bawendi, Synthesis and characterization of nearly monodisperse CdE (E = sulfur, selenium, tellurium) semiconductor nanocrystallites, Journal of the American Chemical Society, 115 (1993) 8706-8715.

[18] D. Norris, M. Bawendi, Measurement and assignment of the size-dependent optical spectrum in CdSe quantum dots, Physical Review B, 53 (1996) 16338-16346.

[19] R. Somers, M. Bawendi, D. Nocera, CdSe nanocrystal based chem-/bio-sensors, Chemical Society Reviews, 36 (2007) 579-591.

[20] S. Mukamel, Principles of nonlinear optical spectroscopy, Oxford, New York, 1995.

[21] T. Brixner, J. Stenger, H. Vaswani, M. Cho, R. Blankenship, G. Fleming, Two-dimensional spectroscopy of electronic couplings in photosynthesis, Nature, 434 (2005) 625-628.

[22] M. Cho, T. Brixner, I. Stiopkin, H. Vaswani, G. Fleming, Two dimensional electronic spectroscopy of molecular complexes, Journal of the Chinese Chemical Society, 53 (2006) 15-24.

[23] V. Klimov, Optical nonlinearities and ultrafast carrier dynamics in semiconductor nanocrystals, Journal of Physical Chemistry B, 104 (2000) 6112-6123.

[24] C. Burda, S. Link, M. Mohamed, M. El-Sayed, The relaxation pathways of CdSe nanoparticles monitored with femtosecond time-resolution from the visible to the IR: Assignment of the transient features by carrier quenching, Journal of Physical Chemistry B, 105 (2001) 12286-12292.

[25] E. McArthur, A. Morris-Cohen, K. Knowles, E. Weiss, Charge Carrier Resolved Relaxation of the First Excitonic State in CdSe Quantum Dots Probed with Near-Infrared Transient Absorption Spectroscopy, Journal of Physical Chemistry B, 114 (2010) 14514-14520.

[26] M. Salvador, P. Nair, M. Cho, G. Scholes, Interaction between excitons determines the non-linear response of nanocrystals, Chemical Physics, 350 (2008) 56-68.

[27] L. McKimmie, C. Lincoln, J. Jasieniak, T. Smith, Three-Pulse Photon Echo Peak Shift Measurements of Capped CdSe Quantum Dots, Journal of Physical Chemistry C, 114 (2010) 82-88.

[28] G. Griffin, S. Ithurria, D. Dolzhnikov, A. Linkin, D. Talapin, G. Engel, Two-dimensional electronic spectroscopy of CdSe nanoparticles at very low pulse power, Journal of Chemical Physics, 138 (2013).

[29] J. Caram, H. Zheng, P. Dahlberg, B. Rolczynski, G. Griffin, A. Fidler, D. Dolzhnikov, D. Talapin, G. Engel, Persistent Interexcitonic Quantum Coherence in CdSe Quantum Dots, Journal of Physical Chemistry Letters, 5 (2014) 196-204.

[30] B. Sun, B.A. Diogo, R. Singh, G.M. Diederich, M.E. Siemens, L.A. Padilha, W.K. Bae, J. Pietryga, V. Klimov, S. Cundiff, Two Dimensional Coherent Spectroscopy of CdSe/ZnS Colloidal Quantum Dots at Cryogenic Temperatures, CLEO: 2015, (2015) JW2A.54.

[31] H. Zheng, J.R. Caram, P.D. Dahlberg, B.S. Rolczynski, S. Viswanathan, D.S. Dolzhnikov, A. Khadivi, D.V. Talapin, G.S. Engel, Dispersion-free continuum two-dimensional electronic spectrometer, Appl. Opt., 53 (2014) 1909-1917.

[32] L. Wang, N. Williams, E. Malachosky, J. Otto, D. Hayes, R. Wood, P. Guyot-Sionnest, G. Engel, Scalable Ligand-Mediated Transport Synthesis of Organic-Inorganic Hybrid Perovskite

Nanocrystals with Resolved Electronic Structure and Ultrafast Dynamics, Acs Nano, 11 (2017) 2689-2696.

[33] V.L. Vadim, I. Pastirk, M. Dantus, Multiphoton intrapulse interference. IV. Ultrashort laser pulse spectral phase characterization and compensation, Opt. Lett., 29 (2004) 775-777.

[34] T. Brixner, T. Mancal, I. Stiopkin, G. Fleming, Phase-stabilized two-dimensional electronic spectroscopy, Journal of Chemical Physics, 121 (2004) 4221-4236.

[35] B. Dabbousi, J. RodriguezViejo, F. Mikulec, J. Heine, H. Mattoussi, R. Ober, K. Jensen, M. Bawendi, (CdSe)ZnS core-shell quantum dots: Synthesis and characterization of a size series of highly luminescent nanocrystallites, Journal of Physical Chemistry B, 101 (1997) 9463-9475.

[36] D. Talapin, A. Rogach, A. Kornowski, M. Haase, H. Weller, Highly luminescent monodisperse CdSe and CdSe/ZnS nanocrystals synthesized in a hexadecylamine-trioctylphosphine oxide-trioctylphospine mixture, Nano Letters, 1 (2001) 207-211.

[37] D. Battaglia, B. Blackman, X. Peng, Coupled and decoupled dual quantum systems in one semiconductor nanocrystal, Journal of the American Chemical Society, 127 (2005) 10889-10897.

[38] C. Burda, S. Link, T. Green, M. El-Sayed, New transient absorption observed in the spectrum of colloidal CdSe nanoparticles pumped with high-power femtosecond pulses, Journal of Physical Chemistry B, 103 (1999) 10775-10780.

[39] K. Zidek, M. Abdellah, K. Zheng, T. Pullerits, Electron relaxation in the CdSe quantum dot - ZnO composite: prospects for photovoltaic applications, Scientific Reports, 4 (2014).

[40] R. Meulenberg, J. Lee, A. Wolcott, J. Zhang, L. Terminello, T. van Buuren, Determination of the Excition Binding Energy in CdSe Quantum Dots, Acs Nano, 3 (2009) 325-330.

[41] C. Wong, G. Scholes, Biexcitonic Fine Structure of CdSe Nanocrystals Probed by Polarization-Dependent Two-Dimensional Photon Echo Spectroscopy, Journal of Physical Chemistry a, 115 (2011) 3797-3806.

6 Conclusions

Colloidal semiconductor quantum dots (QDs), or known as semiconductor nanocrystals, have attracted tremendous attention over the last three decades since first discovered in 1980. Quantum dots are composed of hundreds to thousands of II-VI, III-V, or IV-VI atoms. They are constrained in three dimensions to a spherical shape with diameters in the range of 2-10 nanometers, and display unique optical and electronic properties intermediate between those of bulk material and individual molecules.

In Chapter 1, the quantum confinement effect was discussed using the "particle in a box" model. When the size of the semiconductor nanocrystal is smaller than the exciton Bohr radius, the energy levels in valence band and conduction band are split. The discrete and quantized energy levels in quantum dots are a function of their size, chemical compositions and structures. We can change these parameters to tune the photoelectric properties of quantum dots.

Among all II-VI semiconductor quantum dots, cadmium selenide (CdSe) is found to be of great interest and extensively investigated in the recent years, due to its broad bandgap distribution, familiar physical properties and reliable synthetic procedures. Therefore, CdSe QDs are considered to be the ideal candidates for various potential applications, such as quantum computation, photovoltaic devices, light emitting devices, biological imaging and medical devices. However, many atoms in QDs are present on the surface as a result of the high surface to volume ratio. These surface atoms coordinated with surrounding organic ligands, can "feel" the environment. They can also create surface trap states which facilitate non-radiative exciton decay and thereby lead to luminescence quenching. One of the methods for passivate the surface of QDs is growing shells of another semiconducting material with a larger band gap. In Chapter

2, I synthesized monodispersed CdSe core, CdSe/ZnS core-shell, and CdSe/ZnS/CdSe core-shell-shell quantum dots, via successive ion layer adsorption and reaction method, to explore the surface influence on early time electronic dynamics of QDs.

CdSe QDs has been studied using both linear and non-linear spectroscopies. Specifically, the early time electronic dynamics in CdSe QDs have been measured using two-dimensional electronic spectroscopy (2DES) or transient absorption spectroscopy. The basic theories of non-linear spectroscopy were introduced in Chapter 1. In Chapter 3, I explained the fundamental principles of laser pulse and white light generations, and presented the data acquisition and analysis methods for both 2DES and pump-probe experiment. The projection slice theorem was demonstrated to phase the 2DES.

In Chapter 4, we designed a dispersion-free all-reflective two dimensional electronic spectrometer. Since we used a continuum broadband laser spectrum for the 2DES, it is extremely critical to minimize the non-linear dispersion. We implemented a four mirror system to reflect four pulses separately and control the coherence time precisely without bringing in any color-dependent temporal dispersion. The good optical phase stability and precise coherence time control allow accessing to broader spectral regions. In this chapter, we used this broadband 2DES to probe two different broadly absorbing systems: a large CdSe QDs and Chlorophyll *a* (Ch*la*). The spectral features corresponding to the first three excitons in the CdSe QDs are clearly resolved. Similarly, the Q_x and Q_y bands in Chl*a* can be detected simultaneously. In short, we proved that this broadband 2DES gives us a way to probe highly complex system in the future.

In Chapter 5, the dispersion-free broadband two-dimensional electronic spectroscopy introduced in Chapter 4 was improved and used to probe early time electronic relaxation

dynamics in CdSe core, CdSe/ZnS core-shell, and CdSe/ZnS/CdSe core-shell-shell structures. A white light spectrum with FWHM from 480 to 700 nm was applied to probe these low energy excitons near the band edge. Phasing the two dimensional spectra using pump-probe spectroscopy, I am able to resolve the spectral features of the first two lowest excitons clearly. After plot the cross peak signal intensity against waiting time, I got different relaxation dynamics for these samples. In CdSe core, there is a very strong cross peak at zero waiting time. Then this cross peak decrease dramatically within the first 20 fs, and after that increase slowly. The same feature was observed previously by Griffin and Turner. The CdSe/ZnS/CdSe core-shell-shell structure shows the same trend since the ZnS shell is not thick enough to decouple the CdSe shell from the core. However, CdSe/ZnS core-shell structure shows a different relaxation trace. The signal increases slowly during the early time from 0 to 80 fs, but not decreases at very early time. This difference is reproduced using another pair of CdSe core and CdSe/ZnS core shell QDs with a larger size. I proposed that the surface will influence the two relaxation mechanism, i.e. the Auger-like mechanism and the surface process, leading to different relaxation dynamics at early time between core and core-shell QDs. In other words, the relaxation processes in QDs are affected by the surface environment, such as surface defects or organic ligands.